11-20-2012 12:00 AM

Characterization of Cardiomyopathy in a Mouse Model of Duchenne Muscular Dystrophy (DMD) Using Echocardiography, DCE-CT, and PET-FDG

Seyed Hamed Moazami
The University of Western Ontario

Supervisor
Dr. Lisa Hoffman
The University of Western Ontario

Graduate Program in Medical Biophysics
A thesis submitted in partial fulfillment of the requirements for the degree in Master of Science

Characterization of Cardiomyopathy in a Mouse Model of Duchenne Muscular Dystrophy (DMD) Using Echocardiography, DCE-CT, and PET-FDG

(Spine title: Cardiomyopathy in Dystrophic Mice)

(Thesis format: Monograph)

by

Seyed Hamed Moazami

Graduate Program in Medical Biophysics

A thesis submitted in partial fulfillment
of the requirements for the degree of
Master of Science

The School of Graduate and Postdoctoral Studies
The University of Western Ontario
London, Ontario, Canada

THE UNIVERSITY OF WESTERN ONTARIO
School of Graduate and Postdoctoral Studies

CERTIFICATE OF EXAMINATION

Supervisor

_____
Dr. Lisa Hoffman

Supervisory Committee

_____
Dr. Donna Goldhawk

_____
Dr. Qinping Feng

Examiners

_____
Dr. Maria Drangova

_____
Dr. Tianqing Peng

_____
Dr. Frank Prato

The thesis by

Seyed Hamed Moazami

entitled:

Characterization of Cardiomyopathy in a Mouse Model of Duchenne Muscular Dystrophy (DMD) Using Echocardiography, DCE-CT, and PET-FDG
is accepted in partial fulfillment of the
Requirements for the degree of
Masters of Science

_____
Date

_____
Chair of the Thesis Examination Board

ABSTRACT

Duchenne muscular dystrophy (DMD) is an X-linked recessive neuromuscular disease that is the result of a loss of functional dystrophin, which causes cardiomyocyte fibrosis and death, leading to cardiomyopathy. In this thesis, I have utilized dynamic contrast-enhanced computed tomography (DCE-CT), positron emission tomography-fluorodeoxyglucose (PET-FDG), echocardiography, and traditional histology to longitudinally assess disease progression and degree of cardiomyopathy in a murine model of DMD (mdx:utrn-/-). No significant changes were observed in the blood flow, blood volume, or cardiac volume measured via DCE-CT, nor in standard uptake value (SUV) of glucose as measured by PET-FDG in the left myocardium between and within the two study groups (of mdx:utrn -/- mice and healthy wild-type mice) over time. Our pilot echocardiography study and histological results show possible morphological/architectural and functional changes in affected myocardia of mdx:utrn-/- mice. These findings may provide us with an avenue to longitudinally characterize the progression of cardiomyopathy in the murine model of DMD, mdx:utrn -/- , in addition to providing a potential baseline for a comparison with future therapeutics.

KEYWORDS

Duchenne Muscular Dystrophy, Cardiomyopathy, Dynamic contrast enhanced computed tomography, Positron emission tomography, Echocardiography, Histology quantification, Mdx:utrn-/-, Cardiac, Perfusion, Metabolism

ACKNOWLEDGMENTS

I would like to begin by thanking my supervisor Dr. Lisa Hoffman for her endless support, guidance, and patience. Lisa provided me with such educational experience that will never be forgotten. I also would like to thank my advisory committee Dr. Goldhawk and Dr. Feng, for their guidance. Moreover, I would like to thank my lab member, Kelly Gutpell and all the individuals, whom dedicated their time to help me during my project. I would like to give special thanks to Jennifer Hadway, and Lise Desjardins for assistance with CT and PET scans. I also would like to thank Geron Bindseil for his guidance on PET scans and analysis. Thanks to Drs. Lee and So for their guidance on CT perfusion analysis. Special thanks to Dr. Feng's group (especially Yin Liu) for helping with echocardiography scans and analysis. I would also like to thank Dr. Bureau for his detailed insight and help with statistical analysis.

Most importantly, I would like to thank my family, especially my mom, dad, and my beautiful fiancé for their support, guidance, and endless love and kindness throughout my life.

Thank you

TABLE OF CONTENTS

LIST OF TABLES

LIST OF FIGURES

LIST OF ABBREVIATIONS

DMD	Duchenne muscular dystrophy
Ad	Anterior wall thickness at diastole
ARVD	Arrhythmogenic right ventricular dysplasia
As	Anterior wall thickness at systole
BF	Blood flow
BMD	Becker muscular dystrophy
BV	Blood Volume
Ca	Calcium
Ca(t)	Arterial concentration
DCE-CT	Dynamic contrast enhanced computed tomography
DGC	Dystrophin glycoprotein complex
EF	Ejection fraction
EVS	Extra-vascular space
FDG	Fluorodeoxyglucose
H&E	Hematoxylin and Eosin
IRF	Impulse residue function
IVS	Intravascular space
LOR	Line of response
LV	Left ventricle
LVID	Left ventricular internal diameter
MDX	X-chromosome linked muscular dystrophy
nNOS	Neuronal nitric oxide synthase
Pd	Posterior (septal) wall thickness at diastole
PET	Positron emission tomography
Ps	Posterior (septal) wall thickness at systole
Q(t)	Tissue concentration
ROI	Regions of interest
SAC	Stretch activated channels
SF	Shortening fraction
SUV	Standard uptake value
TDC	Time density curve
US	Ultrasound
XLDC	X-linked Dilated Cardiomyopathy

APPENDIX/ETHICS APPROVAL

CHAPTER 1: INTRODUCTION

1.0 Introduction

Duchenne Muscular Dystrophy (DMD) is an X-linked recessive neuromuscular disease that affects approximately 1 in 3500 males (1-7). It is the second most common single gene disorder in Western countries (8), and it is one of the subcategories of muscular dystrophies, classified as a group of genetic disorders with progressive muscle weakness and wasting. To date, over 30 different types of muscular dystrophies have been identified and described (9).

Duchenne muscular dystrophy is the most widespread form of dystrophy. It is named after the French neurologist, Guillaume Benjamin Duchenne, who first described the disease in 1868 (10). The majority of the clinical features of DMD result from the absence of membrane-bound dystrophin, which brings about a complex chain of events that include skeletal muscle degeneration (11-14), and cardiomyopathy (15-19), the latter of which is the focus of this research study.

Characterization of cardiomyopathy in DMD patients is of great importance, as it is present in over 90% of patients, and greater than 20% of DMD-related deaths are due to cardiac failure (20,21). More specifically, 25% of DMD patients under the age of 6 exhibit pre-clinical cardiac involvement (for a detailed description see section 1.2.2.2). This number rises to 60% for patients between the ages of 6 to 10. Clinically-apparent cardiomyopathy is detectable at around 10 years of age and is present in nearly all the patients by 18 years of age (22).

Due to enhanced ventilatory support, the life expectancy of DMD patients has progressively increased over the years, hence cardiac involvement dominates later stages of care management (23). The advancing age of DMD patients makes cardiomyopathy a high priority in care management, hence there is a critical need to develop non-invasive methods to improve our current fundamental understanding of the progression of the disease. Use of imaging modalities DCE-CT, PET-FDG, and echocardiography, to fulfill this need, is the focus of this thesis.

1.1 The myocardium, and cardiomyocytes

1.1.1 The myocardium and cardiomyocytes

Cardiac muscle (also termed myocardium) is an involuntary striated muscle. Cardiac cells (also termed cardiomyocytes or myocytes) are surrounded by a cell membrane termed the sarcolemma. Cardiomyocytes are attached to each other via intercalated disks (where the sarcolemmal membranes are joined to each other at desmosomes). The presence of gap junctions allows the spread of excitatory signals/action potentials from one cell to another (24). Like skeletal muscle, the myocardium is also comprised of contractile proteins, actin and myosin, which aid in muscle contraction. Furthermore, cardiac muscle requires the presence of extracellular calcium for its depolarization. A contraction involves an action potential that is generated by the sinoarterial and arterioventricular nodes that travels down from the non-contracting cardiomyocytes to contracting cardiomyocytes. The action potential travels along the T-tubules, which are deep invaginations of the sarcolemma, and triggers L-type calcium channels and a subsequent influx of

calcium into the cardiomyocytes. This initial influx of calcium causes further release of calcium (through positive feedback) from the sarcoplasmic reticulum to the cytosol through ryanodine receptors (25,26). Cytosolic calcium binds to troponin C, causing a conformational change and dislocation of both Troponin I and tropomyosin from the actin sites. This allows myosin to attach to actin, and as a result, contraction takes place. The contraction ends through the release of actin from myosin via release of calcium from the tropomyosin complex. Calcium is cleared from the cytosol by the action of a Na^{+}/Ca^{2+} exchanger and through the sarcoplasmic reticulum (SR) ATPase (which takes up the calcium into SR), leading to decreased levels of calcium within the cytosol (26,27).

1.1.2 Cardiomyopathy

Disease of the cardiomyocyte is termed cardiomyopathy. There are four different types of cardiomyopathy. The first type is arrhythmogenic right ventricular dysplasia (ARVD), which is a condition where the myocardium of the right ventricle is partially replaced by fatty and fibrous tissues. This inhibits the proper transmission of the electrical signal in the heart (28). The second type of cardiomyopathy is restrictive cardiomyopathy in which the myocardium loses its ability to relax in between contractions (during diastole). This is due to the rigidity of the cardiac walls (29). The third type of cardiomyopathy is hypertrophic cardiomyopathy which is characterized by thickening of the myocardial wall with disorganized fibers. This condition occurs as result of sacromeres increasing in size, causing thickening of the walls and misalignment of the cardiomyocytes. These

events in turn prevent proper blood pumping and disrupt electrical signals (30,31). Prior to manifestation of clinical symptoms, most boys with DMD go through a hypertrophic cardiomyopathy stage (32). The fourth type is dilated cardiomyopathy and it is the most common form of cardiomyopathy. It is characterized by left ventricular dilation, and a corresponding increase in left ventricular volume. This thinning and stretching of the myocardium causes impairment to the systolic function of the heart (33).

1.2 Dystrophinopathies

1.2.1 General

Dystrophinopathies are recessive forms of muscular dystrophies. They include a spectrum of muscle diseases that occur as a result of a deficiency in or absence of the cytoskeletal protein, dystrophin. In its mildest form, dystrophinopathies involve muscle cramps and isolated quadriceps myopathy (34). However, on the severe end of the spectrum, dystrophinopathies include Becker Muscular Dystrophy (BMD), X-linked Dilated Cardiomyopathy (XLDC), and Duchenne muscular dystrophy (DMD). While XLDC has no skeletal muscle involvement, dilated cardiomyopathy is a common feature in both DMD and BMD. In BMD and DMD, cardiac involvement includes fibrosis and hypertrophy, leading to cardiomyopathy and cardiac failure (detailed description will follow in section 1.2.2.2) (34,35). These characteristics are milder in BMD, due to a mutation in the dystrophin gene that does not cause a shift in the reading frame of the gene. Hence, the dystrophin protein is present but

smaller in size. In contrast, the DMD mutation introduces an early stop codon in the dystrophin gene such that the dystrophin protein is absent (36).

1.2.2 Clinical Features of DMD

1.2.2.1 Skeletal and other manifestations of DMD

Children with DMD often have an unsteady gait and a developmental delay in walking(37). The clearest feature of disease onset is an enlargement of the calf muscles, deltoids, and quadriceps. As the disease progresses, lumbar lordosis becomes more apparent. Muscle weakness, in addition to muscle and joint shortening, also becomes more profound as the disease progresses. Furthermore, severe kyphoscoliosis develops, in addition to thoracic deformities which restrict proper pulmonary airflow (38). The weakening of the intercostal muscles escalates respiratory problems. At later stages of the disease, reduction of total lung capacity is followed by increased residual volume (39).

1.2.2.2 Cardiac Manifestations of DMD

Early stages of cardiomyopathy in patients involve cardiac arrhythmias. Additionally, mitral valve prolapse is observed in over a quarter of affected boys (40,41). Clinically-detectable defects of cardiac function are first apparent in children around 10 years of age, with nearly all patients exhibiting clinically relevant cardiomyopathy by 18 years of age (16,19). Observed defects include impaired myocardial perfusion, reduction in the systolic and diastolic function, and conduction abnormalities. Degenerative changes that include fibrosis and necrosis

as well as disordering of myofilaments have also been observed histologically (19,42-44).

Biopsies and histological analysis of cardiac muscle have shown features that parallel those observed in the skeletal muscle, including replacement of connective tissue with both fibrous and fatty infiltrations. Fibrosis, in particular, has been shown to originate in the outer myocardium involving the most posteriobasal aspect of the outer free wall of left myocardium. Initially, fibrosis is apparent in small areas, but they progressively become more diffuse, and involve most of the outer half of the ventricular wall (19,45,46).

1.3 Dystrophin and Dystrophin Glycoprotein Complex (DGC)

1.3.1 General

Dystrophin is located on the short arm of the X-chromosome at locus Xp21 (7,47,48). It is the largest human gene, containing 2300 kilo-bases and 79 exons that encode 14 kilo-bases of mRNA (49-52). Translated dystrophin protein plays a crucial role in maintaining the integrity of the sarcolemmal membrane. The lack of dystrophin leads to a rapid progression of DMD. Dystrophin is part of Dystrophin Glycoprotein Complex (DGC), which connects the F-actin filaments to the extracellular matrix, and maintains the integrity of the sarcolemma membrane. In addition, it assists with calcium homeostasis, regulating the permeability of the membrane, and protects cardiomyocytes against contraction-induced damage (15,17,53) (Figure 1.1).

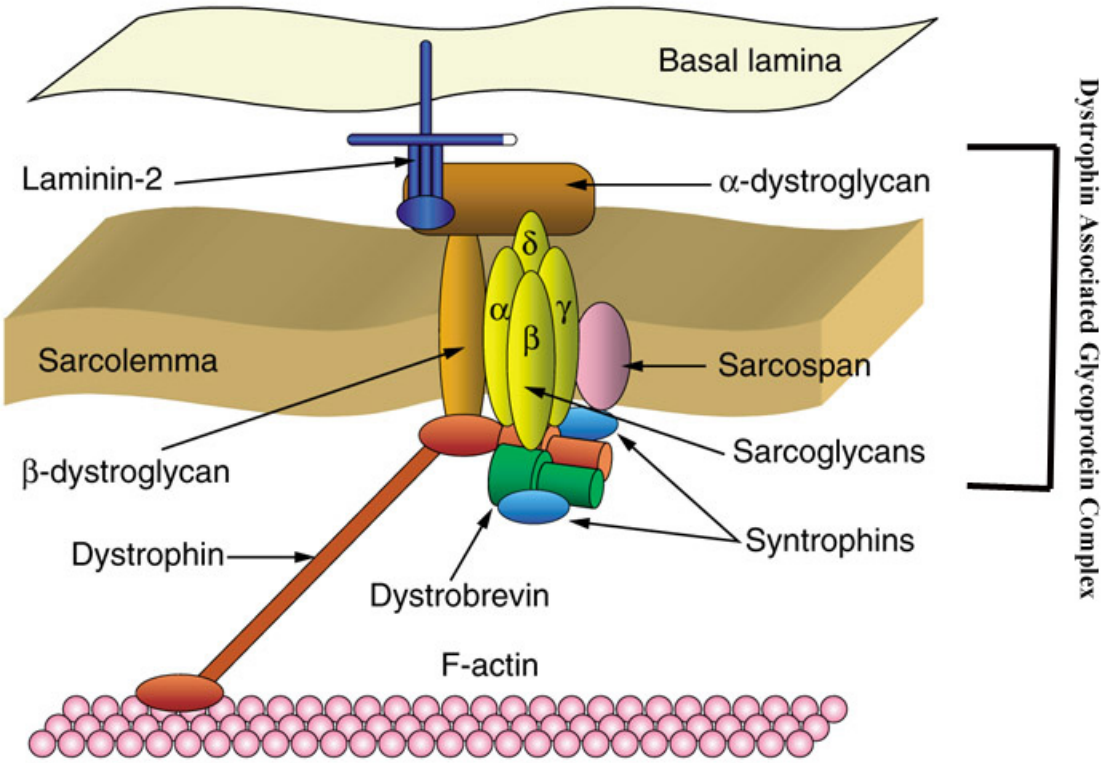

Figure 1.1 Dystrophin and Dystrophin Associated Glycoprotein Complex. Dystrophin is part of Dystrophin Glycoprotein Complex (DGC) binding the F-actin filaments to the extracellular matrix. Figure adapted from Roberts (2001)

1.3.2 Lack of dystrophin from DGC and Sarcolemma

In the absence of dystrophin in the DGC, a cascade of events is initiated that leads to cardiomyocyte death. More specifically, lack of functional dystrophin causes membrane destabilization and tearing due to muscle contractions. Furthermore, lack of functional dystrophin and tearing of the sarcolemma membrane up-regulates stretch activated channels (SAC) and leads to an influx of extracellular calcium and release of intracellular calcium from the intracellular stores (54,55). Increasing

intracellular calcium, in turn, activates calpains which degrade troponin I, and causes contractile dysfunction due to decreased calcium sensitivity. Cardiomyocyte death ensues, allowing infiltrating inflammatory cells and fibroblasts to enter the area to produce fibrosis and formation of scar tissue. It has been shown that in DMD, fibrosis starts at the epicardium of the left ventricular wall and advances toward the endocardium (55,56). Over time, fibrosis regions get thinner, stretch, and lose contractibility, leading to dilated cardiomyopathy. In addition, there is an increase in wall stress and left ventricular volume, as well as a decrease in cardiac output, diastolic relaxation, and contractility (55).

1.4 Animal Models of DMD

1.4.1 General

Homologs of DMD have been found in several species including fish, cats, dogs, invertebrates, and mice. Mammals have always been the preferred choice to study disease conditions of humans, due to similarities in anatomical and metabolic pathways. For example, not only do dogs possess similar body mass to humans, but there is also an extensive homology in disease pathogenesis between humans and dogs (specifically golden retriever DMD). This makes dogs a great choice for studying DMD. However, dogs are not ideal laboratory animals, colonies are expensive to maintain, and they cannot be easily genetically manipulated (57). Dystrophin deficient cats also exhibit cardiomyopathy. However, most

characteristics of DMD are not present in this animal model, preventing them from also being an optimal animal model for studying this disease (57,58).

1.4.2 Mouse models

1.4.2.1 Mdx mice

Mouse models are the most commonly used laboratory model of DMD due to their size and ability to be genetically manipulated. The most common mouse model is the X chromosome-linked muscular dystrophy (mdx) mouse, in which the expression of dystrophin is eliminated due to a point mutation in the dystrophin gene (17,59). These mice exhibit histological signs of muscular dystrophy during their first 6 weeks of life; however, the subsequent course of their disease is different from what is observed in DMD patients. Indeed, mdx mice have near normal life spans, show little weakness, and do not develop severe myofibrosis(19).

Onset of cardiac abnormality is also delayed in mdx mice; as shown via echocardiography and left heart catherization (Quinlan et al. (2004)), fibrosis is less severe in these mice (32). This has been shown to be partly due to the compensatory effects of utrophin, which acts as a homolog to dystrophin (17). Furthermore, studies have shown that regenerating DMD areas with the highest up-regulation of utrophin (normally present in the postsynaptic membrane at the neuromuscular junction) show the least extent of pathological changes such as degeneration and necrosis. When expressed at high levels, utrophin can fully compensate for dystrophin (19,60). These differences have thus limited the utility of

mdx mice as a model for studying both cardiomyopathy and skeletal muscle pathology.

1.4.2.2 Mdx:utrn -/- mice

Mdx:utrn -/- mice not only lack dystrophin, due to a point mutation in the dystrophin gene, but are also null for the utrophin gene (61). Studies have shown that the pathophysiology of the mdx:utrn -/- mouse more closely resembles that in DMD patients (19,62). Common symptoms include dilated cardiomyopathy, reduced growth, diminished mobility, weakness, spinal deformities (kyphosis), ultrastructural neuromuscular and myotendinous junction abnormalities, and premature death (17,19). Through electrophysiology and histological analysis, Grady et al. (1997) have shown that cardiomyopathy is more severe and occurs earlier in mdx:utrn -/- mice relative to mdx littermates (19). Moreover, a study conducted by Chun et al. (2012) used echocardiography to monitor heart function and other parameters, demonstrating that the development of cardiomyopathy in mdx:utrn -/- mice is similar to the pattern seen in DMD patients. Specifically, they have observed a decrease in the ejection fraction and left ventricular fraction shortening as well as an increase in the end diastolic volume, thinning of the ventricular wall, and left ventricular dilation (63,63). Overall, it is of great advantage to use mdx:utrn-/- mice to study cardiac disease progression, since cardiomyopathy develops similarly to that of DMD patients both histologically and functionally.

1.5 Medical Imaging Modalities Used in Characterization of DMD

Medical Imaging is a process whereby visual representations of the body parts, tissues, and organs are created to study its function, anatomy, and biological processes. Early methods of studying pathology and the progression of DMD consisted of blood tests, and painful invasive biopsies. However, recent advances in medical imaging now provide us with an ability to diagnose, monitor, and study disease progression non-invasively. To date, a variety of imaging modalities have been used to study DMD, each with its own strengths and weaknesses. For example, research conducted by Perloff et al. (1984) and Quinlivan et al. (1996) to study alterations in myocardial metabolism, perfusion, wall motion, and cardiac function in DMD patients using radionuclides and positron emission tomography (PET), have identified abnormalities in the myocardium and metabolism/perfusion mismatches (18,44). More specifically, Perloff et al. (1984), used PET to demonstrate that there is an increase in glucose uptake in the posteriolateral and posteriobasal wall of the left ventricle. In addition, Quinlivan et al. (1996), also using PET have shown that there are perfusion defects in the area of inferior, and anterior regions of left ventricle. This study further demonstrates that in the majority of DMD patients, there is a mismatch between perfusion and glucose uptake in the myocardium, suggesting that these differences may be due to myocardial ischemia.

Echocardiography has also been used to measure cardiac function in studies involving DMD patients, demonstrating patterns of cardiac involvement in the disease which encompasses left ventricular dilation and decrease in function (64-67). Previously, echocardiography was used to measure left ventricular posterior wall motion abnormalities in Duchenne muscular dystrophy (32,64-68). A study conducted by Quinlan et al. (2004) has described use of echocardiography to measure the evolution of cardiomyopathy in mdx mice and demonstrated that there are important clinical features that are shared between the mdx mouse model and cardiomyopathy in DMD patients. These shared clinical features include cardiomyocyte hypertrophy and necrosis, as well as cardiac fibrosis (32). Furthermore a study conducted by Chetboul et al. (2004) used tissue Doppler imaging to detect myocardial abnormalities in a dog model of Duchenne muscular dystrophy. They have shown that there is a decrease in systolic and early diastolic myocardial velocity gradient and that the sensitivity of Doppler imaging is higher than conventional method of echocardiography when pre-clinical cardiac abnormalities are detected (69).

In a previous study conducted by our group (Ahmad et al. (2011)), we utilized imaging modalities of DCE-CT and PET-FDG to assess perfusion and glucose metabolism in the skeletal muscle of both mdx and mdx:utrn -/- mice. It was observed, that there is an initial peak followed by a decrease in the blood flow (BF), blood volume (BV) and glucose uptake (9). DCE-CT was utilized based on previous studies showing that in DMD, neuronal nitric oxide synthase (nNOS) mislocalization produces ischemia (70). Thus, measuring BF and BV via DCE-CT may be indicative,

of the degree of ischemia and overall skeletal muscle condition. Healthy muscle readily metabolized glucose; thus reduced 18F-FDG uptake might also be indicative of disease pathology.

There is a necessity for the use of preclinical, small animal models in the area of imaging technology. Use of these models will allow us to better understand disease pathogenesis such that we can intervene and treat disease at an earlier stage or to slow its progression. In this study, the imaging modalities DCE-CT, PET-FDG and echocardiography were utilized to longitudinally study disease progression in the myocardia of mdx:utrn -/- mice, and furthermore, to provide a baseline for comparison when monitoring the success/failure of future therapeutics.

1.5.1 Dynamic Contrast Enhanced Computed Tomography (DCE-CT)

Dynamic contrast enhanced computed tomography (DCE-CT) uses a series of CT scans at the same location to study the distribution of a contrast agent in the myocardium as a function of time. Dynamic CT has become the dominant CT method in clinical evaluation of physiological function (71) . One of the main advantages of functional CT over other modalities, has been its simplicity and accessibility (71).

The intensity of the CT image, which is expressed as a Houndsfield unit, is determined by the efficiency with which the x-ray is attenuated (71,72). In functional CT, the iodine based contrast agent is injected intravenously, and an increase in the attenuation or enhancement of tissue contrast following arrival of the contrast agent is measured (71,73). An Initial data processing step is to subtract the baseline image intensity from the image intensities following arrival of the contrast agent. This subtraction of baseline scans from the scans following arrival of

the contrast agent, provides a time-density curve (TDC) or time-versus-enhancement curve. A baseline scan, followed by series of scans until the clearance of the contrast agent from the tissue, is conducted.

In a DCE-CT study, x-ray iodine based contrast agents are injected via a peripheral vein into the blood stream. Using CT, the tissue concentration, Q(t), and the arterial concentration, Ca(t) are measured (9,71-73). The basis of this technique is dependent on the assumption that contrast enhancement of the region relies on the tracer concentration, and that the tracer is uniformly distributed in the ventricle. Using the appropriate tracer kinetic models in conjunction with acquired data, hemodynamic information in regards to tissue blood flow and tissue blood volume is extracted (9).

The algorithm used in CT perfusion is based on the Johnson Wilson model, a distributed compartmental model with bidirectional flow (72,74). The model divides the myocardium in two principal spaces: the extra-vascular space (EVS) and intravascular space (IVS), which are separated by the permeable capillary endothelium. This model is based on three assumptions. First, there is a homogenous spatial distribution of tracer concentration within the EVS. Second, there is bidirectional diffusion of contrast between EVS and IVS. Third, within capillaries there is axial concentration gradient of contrast, however the radial concentration gradient is negligible. Furthermore, adiabatic approximation, derived by St. Lawrence and Lee (1998), assumes that the EVS contrast concentration changes at slower rate relative to IVS. (9,72) The parametric maps are created using the GE Workstation (GE healthcare) with use of its proprietary software (CT

perfusion, GE Health). The tissue and arterial time enhancement curves are created in the raw data set, where the baseline CT scan is subtracted from each of the CT scans after arrival of the contrast. Enhancement is measured in CT numbers (Hounsfield units) and refers to increase in the attenuation of x-ray due to presence of the contrast agent. The blood flow scaled impulse residue function (IRF) is determined by the deconvolution of the arterial and tissue time enhanced curves (blood flow scaled impulse residue function, (F.R(t)) reflects mass of contrast medium remaining in tissue) (73). Residue function represents the probability that a tracer molecule remains in the cardiac tissue. The height of the blood flow scaled IRF will provide the blood flow and the area under the blood flow scaled IRF will provide the blood volume (Figure 1.2). 2D functional maps of blood flow and blood volume, represented by calculated values from voxels according to a colour scale are produced. This will allow quantification of blood flow and blood volume in the region of tissue of interest.

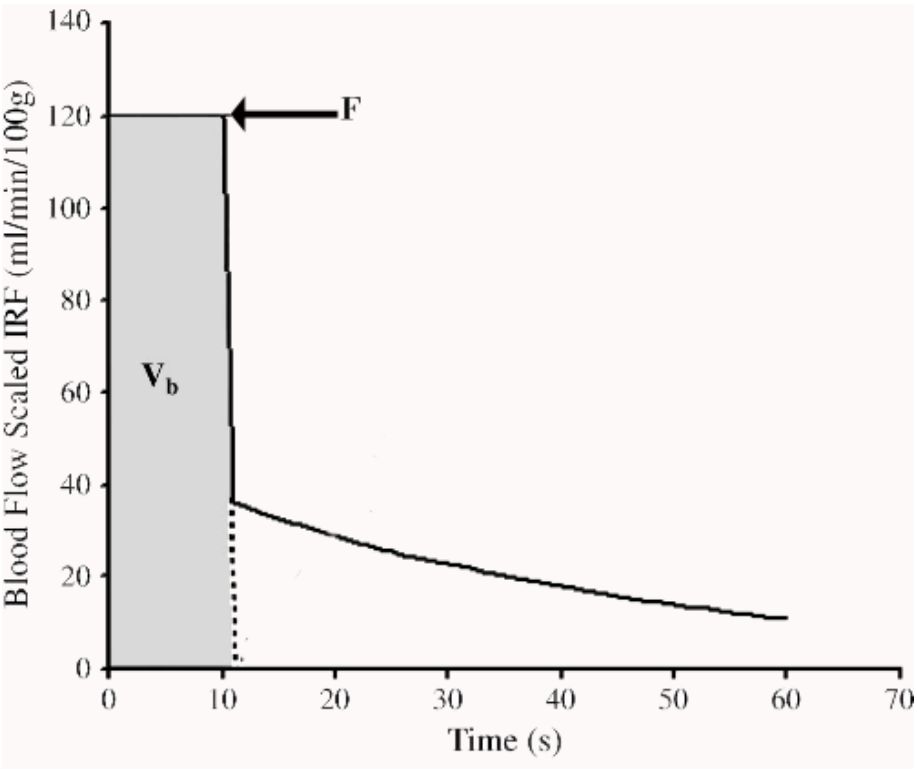

Figure 1.2 Blood flow scaled Impulse residue function, (F.R(t)) reflecting mass of contrast medium remaining in tissue. V_b depicts blood volume and F represents blood flow. Figure adapted from Sahani et. al. (2005) (73)

1.5.2 Positron Emission Tomography (PET)

Positron Emission Tomography (PET) was first introduced in 1975, and has since been used for non-invasive imaging of the heart (75,76). Indeed, PET has been considered to be the gold standard for noninvasive assessment of myocardial viability and perfusion. This is due to its superior sensitivity and its quantitative nature.

In PET, a positron emitting radio-nucleotide labeled chemical compound (in this study ^{18}F-Fluorodeoxyglucose (^{18}F-FDG) was used) is injected into the body. As the radio-nucleotide decays, positrons are emitted, which after traveling for a short distance and losing energy, annihilate with the electron and produce two gamma

rays with energy of 511 keV travelling at opposite directions. These gamma rays are detected on opposite sides by the photomultiplier-scintillating detectors placed in a ring around the body. Scintillating crystals convert the gamma photons to light, which furthermore is multiplied and converted to electrical signal by the photomultiplier tube. To determine whether two signals are from the same source, coincidence processing is performed. If photons do not arrive within temporal pairs (within a timing window of a few nanoseconds), the photons and its subsequent signal are ignored. The coincidence event is assigned to a line of response (LOR), which joins two relevant detectors. The coincidence events are stored in forms of arrays corresponding to the projection through the body and the image is reconstructed using standard tomographic technique (77-79). In PET-FDG studies, the intensity of the image is proportional to uptake concentration of ^{18}F-FDG in the tissue of study, here the myocardium (79).

1.5.3 Echocardiography

Echocardiography (also known as cardiac ultrasound) is a diagnostic technique, which uses ultrasound to measure the anatomy and physiology of the heart. Ultrasound, refers to frequencies that are above 20,000 Hz, and are not audible by the human ear. Cardiac imaging applications use ultrasound frequencies of 1-20 MHz range (80).

In echocardiography, an ultrasound pulse is sent and received via a transducer, which uses piezoelectric material to convert sound to electrical signal and vice versa. As the sound travels though the body, it is partly reflected by the

tissue interphases (where the acoustic properties change), and these reflected pulses are received by the transducer and converted to electrical signal. Since the speed of signal is known in the tissue (to be approximately 1540 m/s in soft tissue), the approximate location can be determined by using time of travel of the pulse. The grey scale display of amplitude over depth information from scan lines is created (80,81). The amplitude of the pulse decreases as it travels through the tissue due to reflection, scatter and absorbance. Higher resolution images can be obtained by increasing the frequency of the pulse; however increasing the frequency would decrease its penetration depth in the tissue.

1.6 Research Outline

The goal of this research project was to longitudinally characterize the progression of cardiomyopathy in the murine model of DMD: mdx:utrn -/- , using non-invasive modalities, PET-FDG, DCE-CT and echocardiography. My three main goals were to:

1. Use DCE-CT to measure longitudinal changes in myocardial perfusion (blood flow and blood volume) in affected (dystrophic) mice, relative to healthy wild-type control mice.
2. Use positron emission tomography (PET-^{18}FDG) to longitudinally measure changes in glucose metabolism in affected myocardia.
3. Use echocardiography to compare the morphological/architectural and functional changes in affected myocardia.

CHAPTER 2: MATERIALS AND METHODS

2.1 Animal Models of Duchenne Muscular Dystrophy

All animal protocols were approved by the Institutional Animals Ethics Committee, University of Western Ontario, and experiments were conducted in accordance to the guidelines of the Canadian Council of Animal Care (CCAC) (animal use protocol approval letter attached in appendix). Wild-type C57BL/6 mice were purchased from Charles River Laboratory International, Inc (Wilmington, MA) at 5-7 weeks of age. Mdx:utrn heterozygote (+/-) mice (generously provided by Robert Grange, Virginia Polytechnic Institute and State University, although originally generated by Mark Grady and Josh Sanes at Washington University, St. Louis) were bred to generate mdx:utrn -/- mice lacking both utrophin and functional dystrophin. Only males were used in the study. Two groups of mice were used: (1) wild-type, (2) mdx:utrn -/-. For the CT and PET experiments, 5 mice were enrolled in each group and scanned bi-weekly starting at 5-7 weeks of age for up to 16-21 weeks of age or until their death. For the echocardiography pilot study, 2 mice were enrolled in the mdx:utrn -/- group and 5 were enrolled in the wild-type group. Each mouse was scanned at two time points: 5-7 weeks of age, and 15-17 weeks of age.

2.2 DCE-CT, PET-FDG, and Echocardiography

2.2.1 DCE-CT, PET-FDG

Mice in both groups (wild-type, mdx:utrn -/-) were enrolled in the study at 5-7 weeks of age. Baseline values were obtained for both micro (μ) PET and clinical CT with the initial scan of each mouse. Mice were subsequently imaged (with the aid of Jennifer Hadway, and Lise Desjardins, Lawson Research Institute (LRI)) for up to 21 weeks of age (Figure 2.1). During each imaging session, mice were first anesthetized with 3-4% isoflourane and then maintained with a 1.5% oxygen-balanced isoflourane mixture, delivered at rate of 1ml/min. The mice were imaged while in a prone position. Images were focused on the heart. For PET-FDG study analysis of regions of interest (ROI) were placed in the area of the lateral, inferior, septal, and anterior walls of the left myocardium of the left ventricle (Figure 2.2). For DCE-CT study, the region of the anterior wall of the left myocardium was removed due to high cardiac wall motion. These ROIs were chosen based on the standards reported by American College of Cardiology, and previous studies by Quinlivan et al. 1996 (44,82). Data acquired for each mouse over the course of the study were normalized to baseline to remove the animal's biological variability, hence allowing us to assess the longitudinal changes between the two groups of mice.

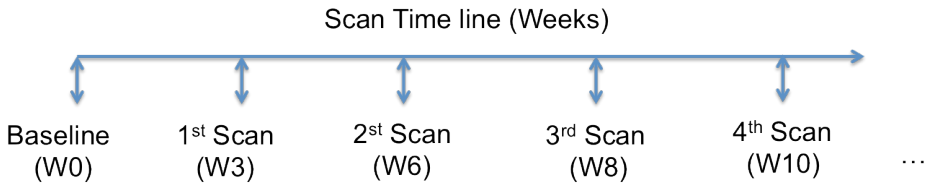

Figure 2.1: Scan Time line for CT and PET**.** Mice in two groups were enrolled at baseline (5-7 Weeks of age), and were imaged once every two weeks for up to 21 weeks of age.

2.2.2 Echocardiography

Mice in wild-type and mdx:utrn -/- groups were enrolled at 5-7 weeks of age. Mice were scanned at two time points; (1) The first scan was conducted at 5-7 weeks of age, and (2) the second scan was conducted at 15-17 weeks of age. During each scanning session, anesthesia was performed with a 3-4% isoflourane and then maintained with a 1.5% oxygen-balanced isoflourane mixture, delivered at rate of 1ml/min. Mice were then placed on a heated platform with electrocardiogram contact pads while in a supine position. Dipilatory cream was placed on each mouse's chest and removed after 2 minutes to remove the hair. Ultrasound gel was subsequently placed on the chest of the anesthetized mouse and different parameters of the heart were measured (will be discussed in later sections) to assess cardiomyopathy and overall heart function.

2.3 DCE-CT

2.3.1 Measurement of Cardiac Blood Flow and Blood Volume

Two parameters of perfusion (blood flow and blood volume) were analyzed in this study for each mouse. 2 cm thick slab (containing the heart), separated into sixteen 1.25mm thick slices at 320μm resolution was scanned repetitively using a Clinical GE scanner. The scan was divided into two phases. The first phase consisted of 24 times exposure of 0.4 seconds with prep time of 1s followed by 12 times exposure of 0.4 seconds with 14.6 s prep time. Mice were injected with contrast agent via tail vein catheter 5 seconds into the first scan. Conray 43 contrast agent diluted to 50% with sterile saline was injected, at 0.2 mls volume and 2 ml/min rate for mice weighting more than 20g and 0.15 mls volume for mice weighting less than 20g, using an infusion pump (New Era Pump System Inc) that was triggered by the CT scanner. Blood flow (BF) and blood volume (BV) maps were subsequently reconstructed using the GE CT perfusion software, which is based on the Johnson Wilson model with adiabatic approximation (9,72-74). A tissue density value of 2.5 was used. Regions of interest (ROI) were placed in the lateral, inferior, septal walls of left myocardium were used to extract the BF and BV values (Figure 2.2 and Figure 2.3). A ROI was not placed with within anterior wall of left myocardium due to high cardiac wall motion. Values of BF and BV for each mouse was normalized to its baseline in order to remove biological variability. The values from mice respective to their own group and weeks were then averaged.

2.3.2 Measuring cardiac volume via CT

Cardiac volume was also calculated using high resolution CT scans previously obtained for the two mice groups. Area was measured using the GE Workstation (GE Healthcare) with use of its software (CT Perfusion™, GE HealthCare). For each scan, the slices containing the heart were chosen and, using a hand drawing tool, the heart boundary was outlined and the area containing the heart was measured. Cardiac volume was calculated using a slice thickness value of 1.25mm and areas measured (in mm^2). This was done for each time point. The values were then normalized to baseline and averaged for each of the two groups to measure potential changes in the cardiac volume for the two groups in time.

2.4 PET-FDG for measurement of glucose metabolism

In this PET study, the radioactive tracer ^{18}F-FDG (fluorodeoxyglucose) was used to measure glucose metabolism. Mice were injected via tail-vein catheter with 300-400 μCi of ^{18}F-FDG. After 45 min to 1 hour of uptake time, static scans were acquired using a μPET scanner (GE Healthcare, Explorer Vista DR) at a photopeak of 250-700 keV for a period of 30 minutes. Images were subsequently reconstructed using 3D Fore-2D OSEM algorithm and corrected for scatter and random coincidences, into twenty-six, 1.75 mm thick slices at a transaxial resolution of 1.6 mm. A 5 cm diameter water phantom containing a known amount of F-18 activity was scanned with μPET to measure the sensitivity factor. This value was subsequently used for converting counts in reconstructed PET images to activity (in MBq). ROIs were drawn in the regions of lateral, inferior, septal, and anterior walls

of the left myocardium to obtain the mean value/pixel (Figure 2.2). These values were then converted to a standard uptake values (SUV) using the formula below (Equation 1 and 2). SUV values were normalized to baseline to remove biological variability. Furthermore the values from mice respective to their own group and weeks were then averaged.

$$SUV = \frac{\frac{mean\_value/pixel}{phantom\_correction\_factor}}{\frac{amount\_of\_radioisotope\_at\_start\_of\_scan(MBq)}{mouse\_weight(g)}} \quad \textbf{...Equation 1}$$

$$Phantom\_correction\_factor = \frac{mean\_value/pixel(phantom)}{\frac{total\_ativity\_in\_phantom(MBq)}{volume(ml)}} \quad \textbf{...Equation 2}$$

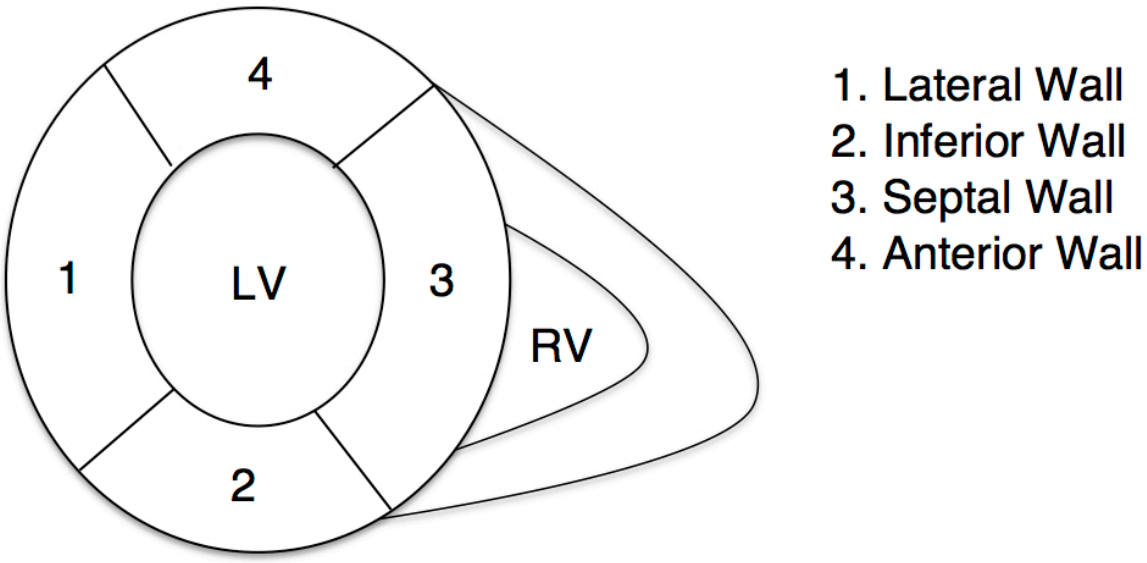

Figure 2.2: Region of analysis used for PET and CT. Areas represent lateral wall, inferior wall, septal wall, and anterior wall of the left myocardium. Left and right ventricles are also shown. For CT the region of anterior wall is avoided due to high cardiac wall motion.

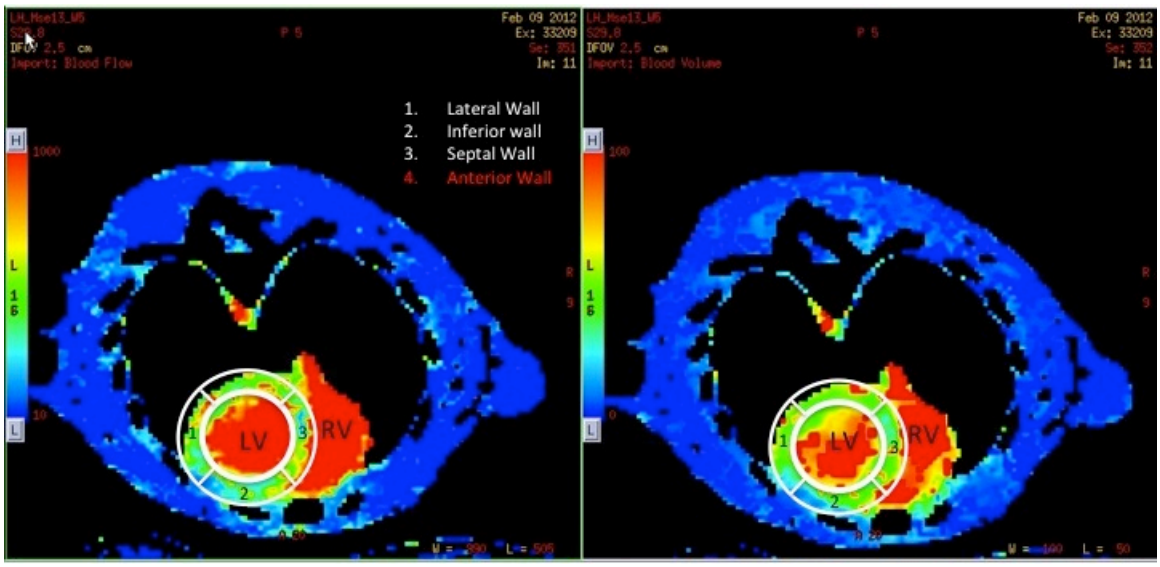

Figure 2.3: Sample DCE-CT image. Left: blood flow. Right: blood volume. Axial slices using DCE-CT of cardiac of a wild-type mouse. White regions represent the regions of analysis, which represent lateral wall, inferior wall, septal wall of left myocardium. For CT, the region of anterior wall is avoided due to high cardiac wall motion.

2.5 Echocardiography for measurement of cardiac anatomy and blood flow

All echocardiography and analysis was conducted with aid of Yin Liu (Dr. Qingping Feng's group at the University of Western Ontario). Echocardiography was performed using a Vevo 2100 High Frequency Ultrasound scanner (Visual Sonics Inc., Toronto, Canada). The ultrasound probe used was MS-550D, operating at 40 MHz with an axial resolution and lateral resolution of 40 μm and 80 μm, respectively. Images were obtained according to echocardiography guidelines using M-mode and B-Mode. Quantitative measurements were performed using the integrated analytical software of the scanner. The following parameters were measured: (1) left ventricular internal diameter (LVID) at both systole and diastole,

(2) anterior and septal (posterior) wall thickness at both systole and Diastole, (3) ejection fraction (EF) and (4) shortening fraction (SF) (Figure 2.4). Ejection fraction is the volumetric fraction of blood that is pumped out of the left ventricle during each beat, and is defined as (LV diastolic volume –LV systolic volume)/ LV diastolic volume. Shortening fraction is the measurement of the change in the diameter of left ventricle and is defined as (LVID $_{(at\ diastole)}$-LVID $_{(at\ Systole)}$)/LVID $_{(at\ diastole)}$. Both EF and SF were used for assessment of ventricular performance.

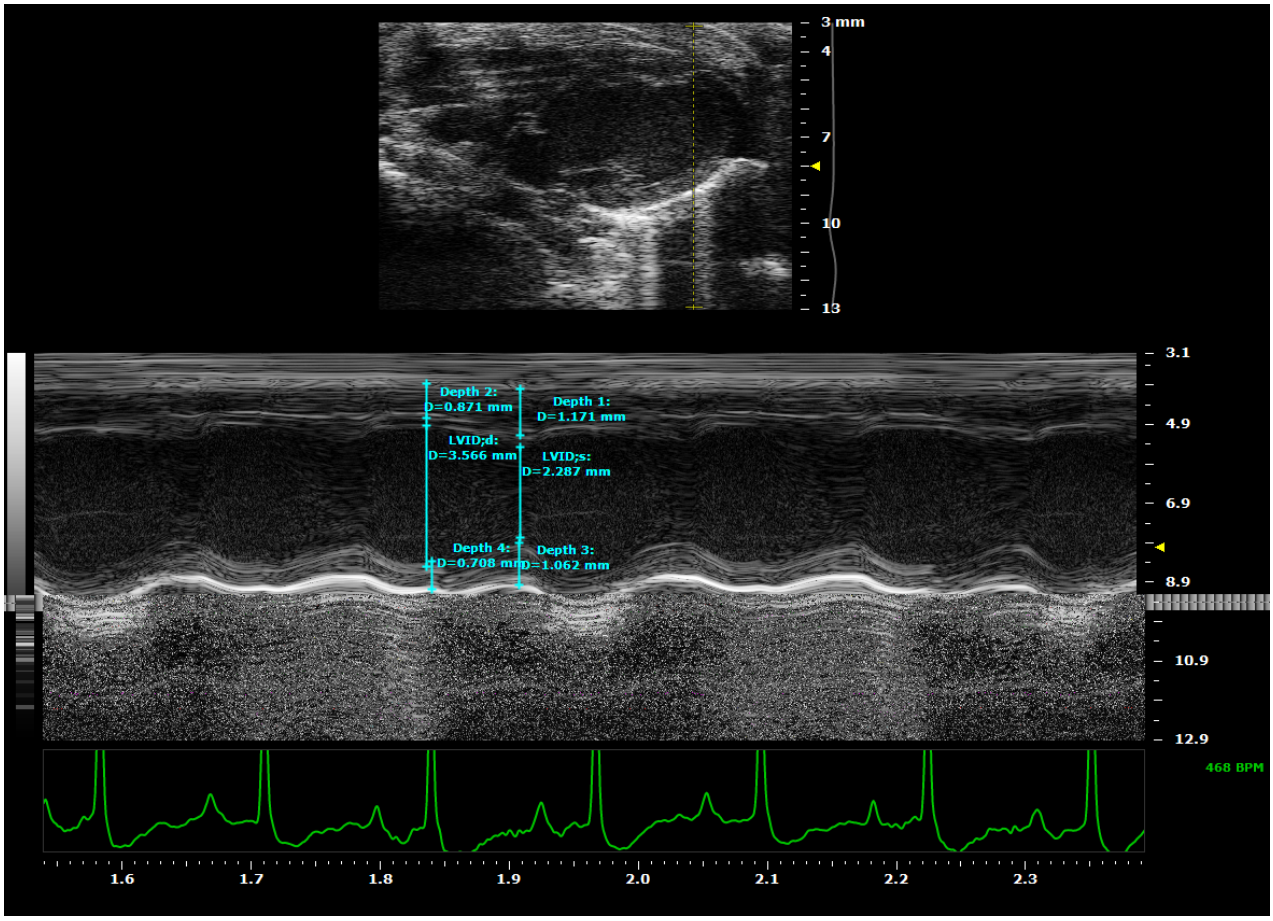

Figure 2.4: Sample M-mode echocardiography scan of heart of wild-type mouse. Measured parameters were; Anterior wall thickness at systole and diastole (Depth 1 and Depth 2), posterior wall (septal wall) thickness at systole and diastole (Depth 3 and 4), and left ventricular internal diameter (LVID) at systole and diastole.

2.6 Histological Analyses

Histology was performed at two time points: (1) baseline and (2) at the termination of the study. Three mdx:utrn -/- mice at end point, 2 mdx:utrn -/- mice at baseline, and 3 wild-type mice for both time points were used. Immediately following euthanasia, hearts were removed and placed in 10% formalin for a minimum of 48 hours. Fixed hearts were then cut in 2 or 3 axial sections (depending on heart size) then were embedded in paraffin. Five mm-thick sections were subsequently cut and sent to the Molecular Pathology Core Facility at the Robarts Research Institute (RRI) (London, Canada) to be stained with Hematoxylin and eosin (H&E) and Masson's trichrome staining. H&E staining was used to quantify hypertrophy and Masson's Trichrome staining was used to quantify fibrosis as previously done by Xiang et al. (2009) and Gao et al. (2003) (83,84).

2.6.1 Quantifying Fibrosis

Quantifying fibrosis was conducted in trichrome stained heart sections using Zeiss Axioskop, and Northern Eclipse Software (V7.0, Empix Imaging Inc.). Using a 40X magnification power, 3 sub-region snapshot images were obtained from each region of lateral wall, inferior wall, septal wall, and anterior walls of the left myocardium. Using ImageJ (Version1.45I) software, areas encompassing the fibrosis regions were outlined and measured, and the ratio of total fibrosis area over total area of each sub-region was calculated. The ratio of fibrosis for each of the 4 regions of the myocardial wall was calculated by averaging the ratio of in corresponding sub-

regions. Overall fibrosis ratio was calculated by averaging the ratio of fibrosis of the 4 regions (83,84).

2.6.2 Quantifying cell size

Hypertrophy in the H&E stained sections was also quantified using a Zeiss Axioskop, and Northern Eclipse Software (V7.0, Empix Imaging Inc). Using a 40X magnification power, 3 sub-region snapshot images were obtained from each region of the lateral wall, inferior wall, septal wall, and anterior walls of the left myocardium. Using ImageJ (Version1.45I) software, the short axis length of 20 cardiomyocytes was measured in each sub-region and averaged (cell's short axis length was used for quantification of cell size). Assessment of hypertrophy in each region of the left myocardium was done through averaging the cell size measurements for its corresponding region. These values were then averaged.

2.7 Data Analysis

All statistics were performed with the aid and guidance of Dr. Yves Bureau (Lawson Health Research Institute). Statistical analyses were performed using SPSS software package for Mac (SPSS Inc, V20.0), and Graphpad Prism software package for Mac (Graphpad Software Inc, V5.0a). To identify significance difference in BF, BV, and SUV parameters within the 2 groups of mice over time, and between the two groups of mice over time, a repeated measures two-way ANOVA (mixed-model) with Bonferroni post-test was performed. Significance differences in the two groups of mice at end point of histology were measured using an unpaired t-test. Low sample

size of mdx:utrn -/- in echocardiography and baseline of histology prevented from inferring statistical analysis.

CHAPTER 3: RESULTS

3.1 A Kaplan Meier survival curve demonstrates that the lifespan of mdx:utrn -/- mice is significantly shorter than wild-type mice

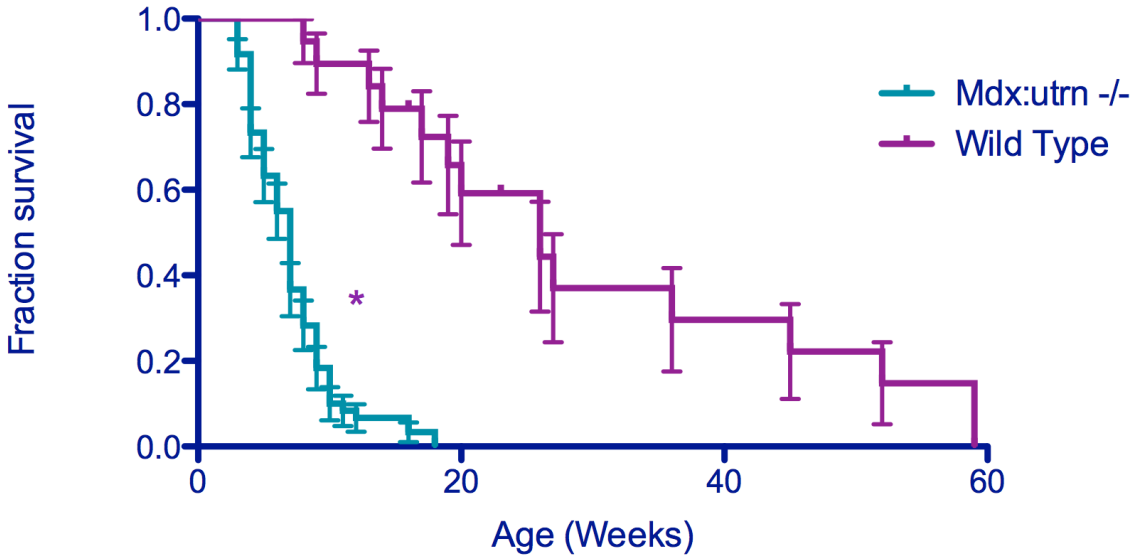

Figure 3.1: Kaplan-Meier survival curve of wild-type and mdx:utrn -/- mice. Mice that were sacrificed at specific histological time points were not included in the Kaplan-Meier survival curve. Data was collected over 2 year period. n=18 for wild-type and n=62 for mdx:utrn -/- mice were used. Y-axis depicts the fraction of survival with a value of 1 depicting 100% survival. The x-axis depicts the age of the mice in weeks. LOG Rank (Mantel-Cox) statistical test found significant difference between the two groups ($P<0.0001$)

In this study, I used a Kaplan Meier curve to assess whether there were significant differences in the lifespan of the mdx:utrn -/- mice relative to healthy wild type mice. As shown in Figure 3.1, the survival fraction of mdx:utrn-/- and wild-type mice by 19 weeks of age were 0 and 0.658 respectively. Median survival of mdx:urtn -/- and wild-type mice were 7 and 26 weeks respectively.

3.2 Dynamic contrast enhanced computed tomography (DCE-CT) demonstrates that myocardial perfusion is not affected in the mdx:utrn-/- mice relative to healthy wild-type mice.

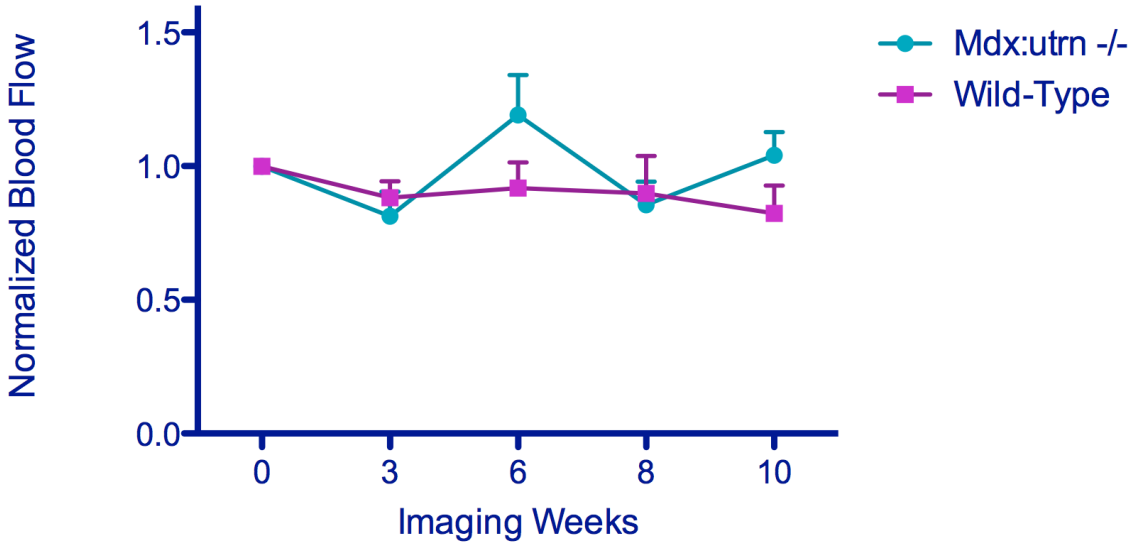

Figure 3.2a: Normalized blood flow analysis in the left ventricular myocardium of wild-type and mdx:utrn -/- mice. Data was collected over a 10-week period and mice were enrolled in study at 5-7 weeks of age (baseline scan (w0)). Repeated measures two-way Anova (mixed-model) with Bonferroni post-test showed no significance in-between and within the groups. Each value represents the mean of the normalized blood flow values for each group at each time point. Error bars represent the standard error of the mean for each group at each time point.

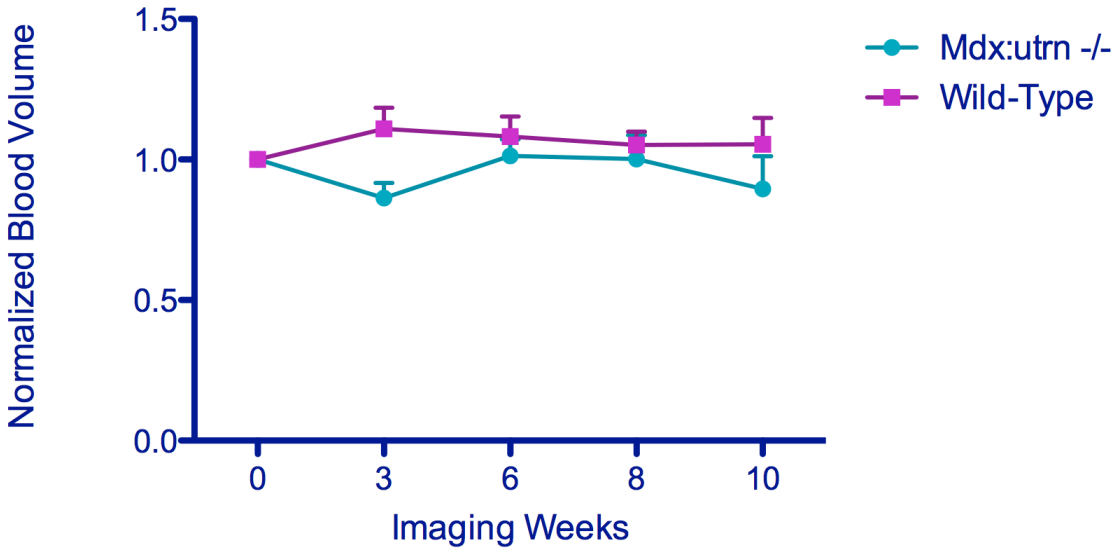

Figure 3.2b: Normalized blood volume analysis in the left ventricular myocardium of wild-type and mdx:utrn -/- mice. Data was collected over a 10 weeks period and mice were enrolled in study at 5-7 weeks of age (baseline scan (w0)). Repeated measures two-way Anova (mixed-model) with Bonferroni post-test showed no significance in-between and within the groups. Each value represents the mean of the normalized blood volume values for each group at each time point. Error bars represent the standard error of the mean for each group at each time point.

Given reports of longitudinal change in the blood flow and blood volume in the skeletal muscle of mdx:utrn-/- mice vs wild-type mice (Ahmad et al. 2011), I sought to assess changes in the ventricular myocardium perfusion (BF and BV). As illustrated in Figure 3.2 a there is no significant difference between the healthy wild-type mice and the mdx:utrn-/- mice at baseline (W0), or over a 10 weeks time period. Blood flow was similarly unaffected (Figure 3.2b).

3.3 Cardiac Volume is also unaffected in mdx:utrn -/- mice as assessed by DCE-CT

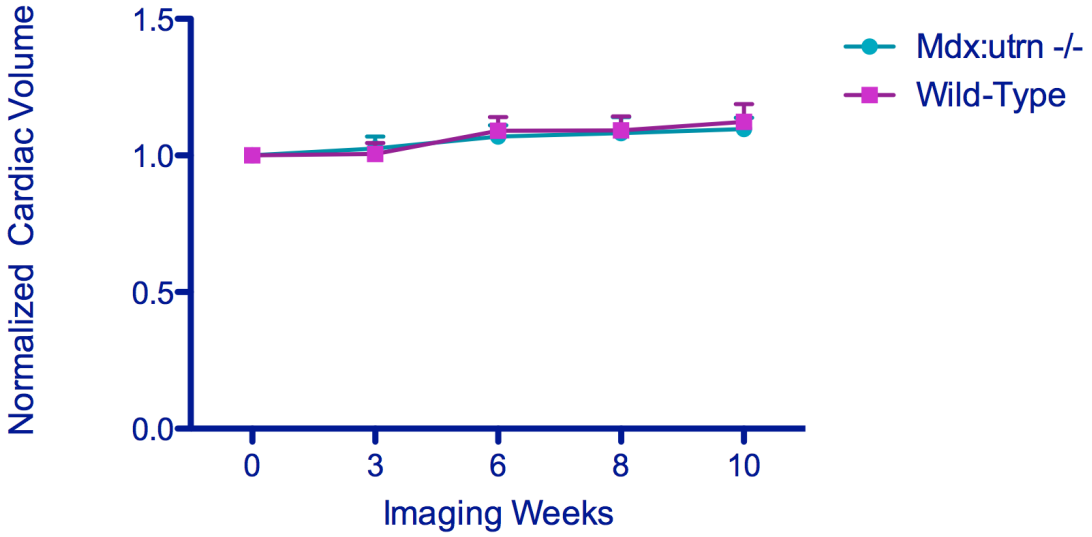

Figure 3.3: Normalized cardiac volume measurement of the wild-type and mdx:utrn -/- mice. CT data was used which was collected over 10 weeks period and the mice were enrolled in study at 5-7 weeks of age (Baseline (W0)). Repeated measures two-way Anova (mixed-model) with Bonferroni post-test showed no significance in-between and within the groups. Each value represents the mean of the cardiac volume values for each group at each time point. Error bars represent the standard error of the mean for each group at each time point.

Normalized cardiac volume measurement via CT does not show significant differences between the healthy mice and mdx:utrn -/- mice (Figure 3.3). As shown mdx:utrn -/- normalized cardiac volume follows similar trend observed in the wild-type.

3.4 Positron Emission tomography (PET-FDG) demonstrates that glucose metabolism is unaffected in the mdx:utrn-/- mice relative to healthy wild-type mice.

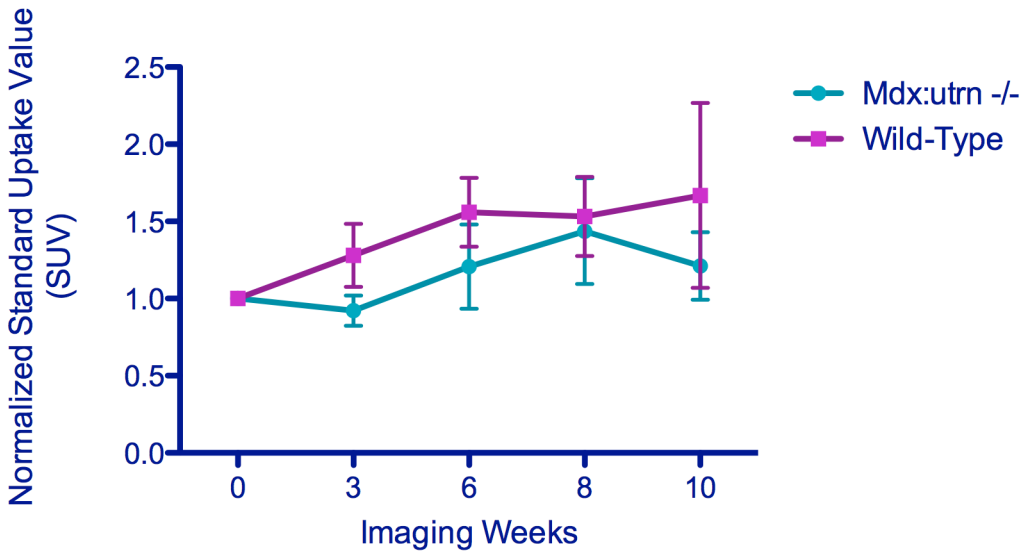

Figure 3.4: Normalized standard uptake value (SUV) of PET-FDG in left ventricular myocardium of wild-type and mdx:utrn -/- mice. Data was collected over a 10 weeks period and mice were enrolled in study at 5-7 weeks of age (baseline scan (w0)). Repeated measures two-way Anova (mixed-model) with Bonferroni post-test showed no significance in-between and within the groups. Each value represents the mean of the normalized SUV values for each group at each time point. Error bars represent the standard error of the mean for each group at each time point.

Given reports of longitudinal change in the glucose uptake in the skeletal muscle of mdx:utrn-/- mice vs. wild-type mice (Ahmad et al. 2011), I sought to assess changes in the ventricular myocardium glucose uptake . As illustrated in Figure 3.4 there was no significant difference between the healthy wild-type mice and the mdx:utrn-/- mice at baseline (W0), or over a 10 weeks time period.

3.5 Pilot Echocardiography shows decrease in the cardiac function of mdx:utrn-/- mice compared to healthy wild-type mice.

Table 1. Echocardiograph data for mdx:utrn-/- and wild-type mice at 5-7 (baseline), and 15-17 weeks of age (endpoint). N=5, and n=2 was used for wild-type and mdx:utrn-/- mice respectively.

	5-7 Weeks of age		15-17 Weeks of age	
	Wild-type (n=5)	**Mdx:utrn -/- (n=2)**	**Wild-type (n=5)**	**Mdx:utrn -/- (n=2)**
LVID'd(mm)	3.7294	3.369	3.1252	2.981
LVID's(mm)	2.41336	2.35	1.8992	2.559
Ad(mm)	0.9364	0.883	0.7884	0.694
As(mm)	1.2852	1.2545	1.1432	0.844
Pd(mm)	0.7514	0.9605	0.7786	0.939
Ps(mm)	1.1596	1.3675	1.0726	1.048
EF(%)	62.5492	58.5815	72.1582	31.3575
FS(%)	33.168	30.2285	40.1508	14.155

LVID'd: Left ventricular internal diameter (diastole), LVID's: Left ventricular internal diameter (systole), Ad: Anterior wall thickness (Diastole), As: Anterior wall thickness (sytole), Pd: Septal (posterior) wall thickness (diastole). Ps: Septal (posterior) wall thickness (systole), EF: Ejection Fraction, FS: Fractional Shortening

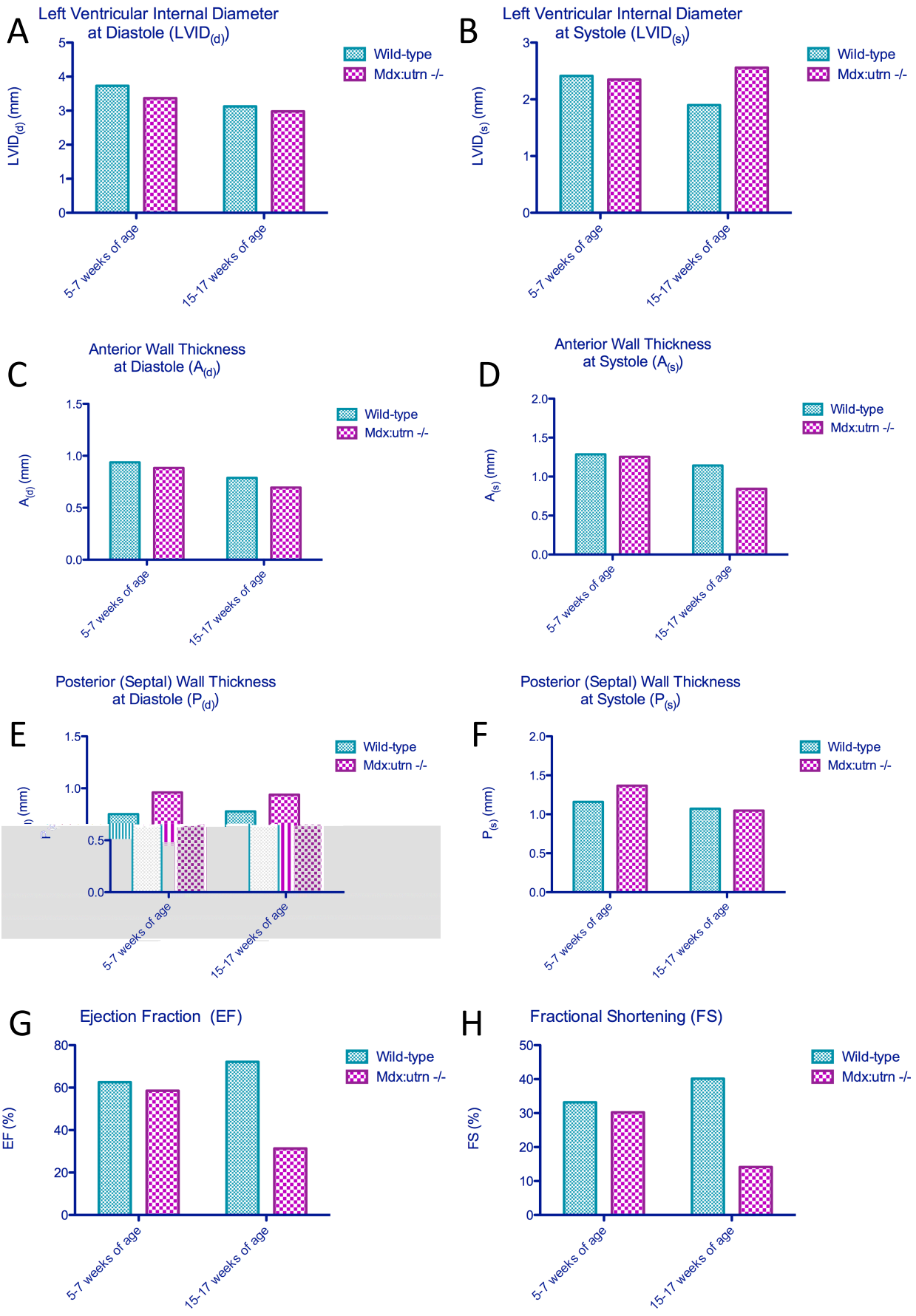
A
Left Ventricular Internal Diameter at Diastole (LVID(d))
LVID(d) (mm)
Wild-type
Mdx:utrn -/-
5-7 weeks of age
15-17 weeks of age
B
Left Ventricular Internal Diameter at Systole (LVID(s))
LVID(s) (mm)
C
Anterior Wall Thickness at Diastole (A(d))
A(d) (mm)
D
Anterior Wall Thickness at Systole (A(s))
A(s) (mm)
E
Posterior (Septal) Wall Thickness at Diastole (P(d))
F
Posterior (Septal) Wall Thickness at Systole (P(s))
P(s) (mm)
G
Ejection Fraction (EF)
EF (%)
H
Fractional Shortening (FS)
FS (%)

Figure 3.5: Echocardiograph trend data for mdx:utrn-/- and wild-type mice at 5-7 (baseline), and 15-17 weeks of age (endpoint). N=5, and n=2 was used for wild-type and mdx:utrn-/- mice respectively. A) Left ventricular internal diameter at diastole. B) Left ventricular internal diameter at systole. C) Anterior wall thickness at diastole. D) Anterior wall thickness at systole. E) Posterior (septal) wall thickness at diastole. F) Posterior (septal) wall thickness at systole. G) Ejection fraction. H) Fractional shortening

Echocardiography parameters measurements are of left ventricular internal diameter (LVID) at systole and diastole, anterior and septal (posterior) wall thickness at systole and diastole, ejection fraction (EF) and fractional shortening (FS) for the two groups of mdx:utrn -/- and wild-type mice at two time points of 5-7 weeks of age (baseline) and 15-17 weeks of age (endpoint) are depicted in table 1 and Figure 3.5. Low sample size in our mdx:utrn -/- group prevented inference of statistical relevance. Overall, I observed an increasing trend in left ventricular internal diameter at systole from the first time points of 5-7 weeks of age (baseline) to second time point of 15-17 weeks of age (end-point of study), whereas decreasing trend was observed in the wild-type mice (Figure 3.5B). FS and EF were observed to have increasing trend in the wild-type mice, however decreasing trend were observed in these two echocardiography parameters in mdx:utrn-/- mice from baseline to end-point of study (Figure 3.5 G&H).

3.6 Histology

3.6.1 Fibrosis quantification shows significantly higher fibrosis in the left myocardium mdx:utrn-/- mice vs. healthy wild-type mice at termination of study.

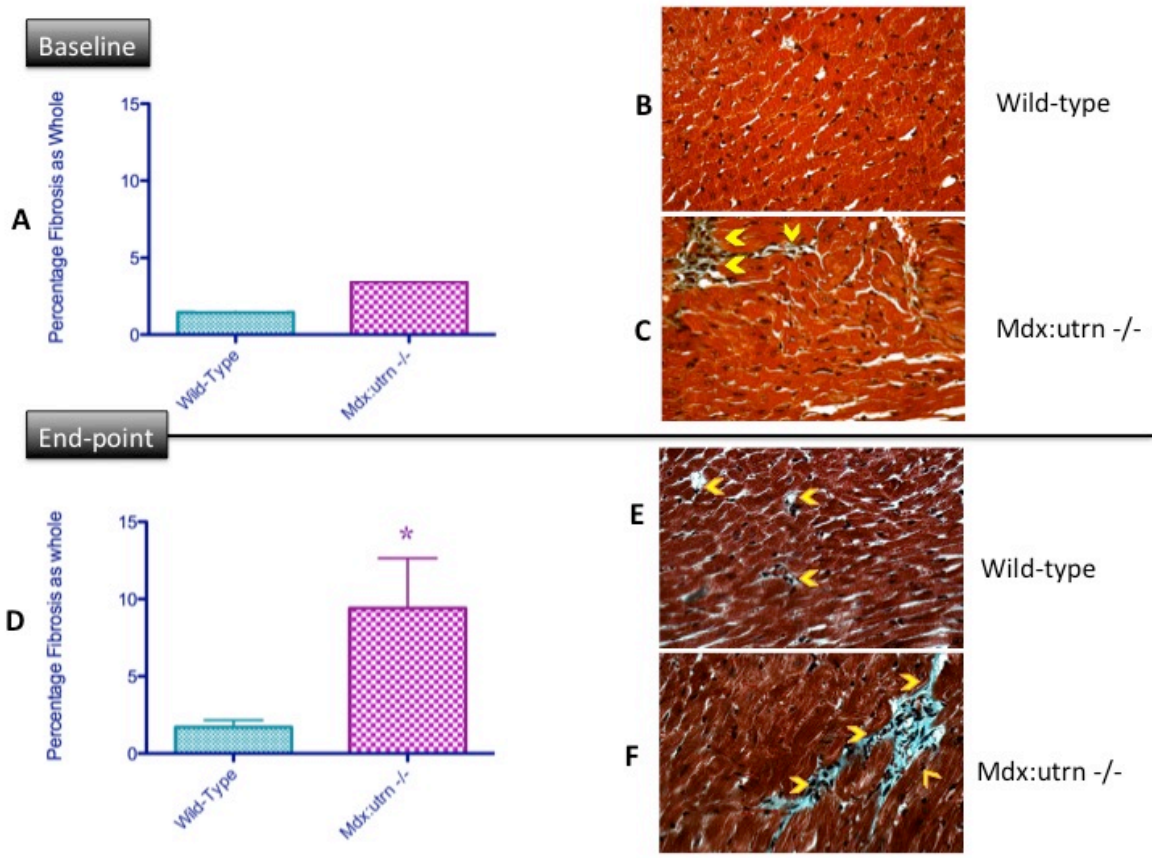

Figure 3.6: Cardiac Fibrosis Quantification. Baseline (n=2 for mdx:utrn-/- and n=3 for wild-type). Endpoint (n=3 for mdx:utrn-/- and n=3 for the wild-type) A) Quantification of cardiac fibrosis in mdx:utrn -/- and wild-type mice sacrificed at baseline. Low sample size in our mdx:utrn -/- group prevented inference of statistical relevance B) Trichrome stained images of the left myocardium of wild-type mouse (taken at baseline) under 40X magnification. C) Trichrome stained images of the left myocardium of mdx:utrn-/- mouse (taken at baseline) under 40X magnification. Yellow arrow tips point to areas of fibrosis. D) Quantification of cardiac fibrosis in mdx:utrn -/- and wild-type mice sacrificed at end of study (endpoint). Unpaired T-test shows significantly higher fibrosis in the mdx:utrn -/- mice compared to healthy wild-type mice ($P<0.05$). E) Trichrome stained images of the left myocardium of wild-type mouse (taken at endpoint) under 40X magnification. Yellow arrow tips point to areas of fibrosis. F) Trichrome stained images of the left myocardium of mdx:utrn-/- mouse (taken at endpoint) under 40X magnification. Yellow arrow tips depicts areas of fibrosis.

3.6.2 Cell size measurement (Hypertrophy assessment) shows significantly increased cell size at endpoint of study

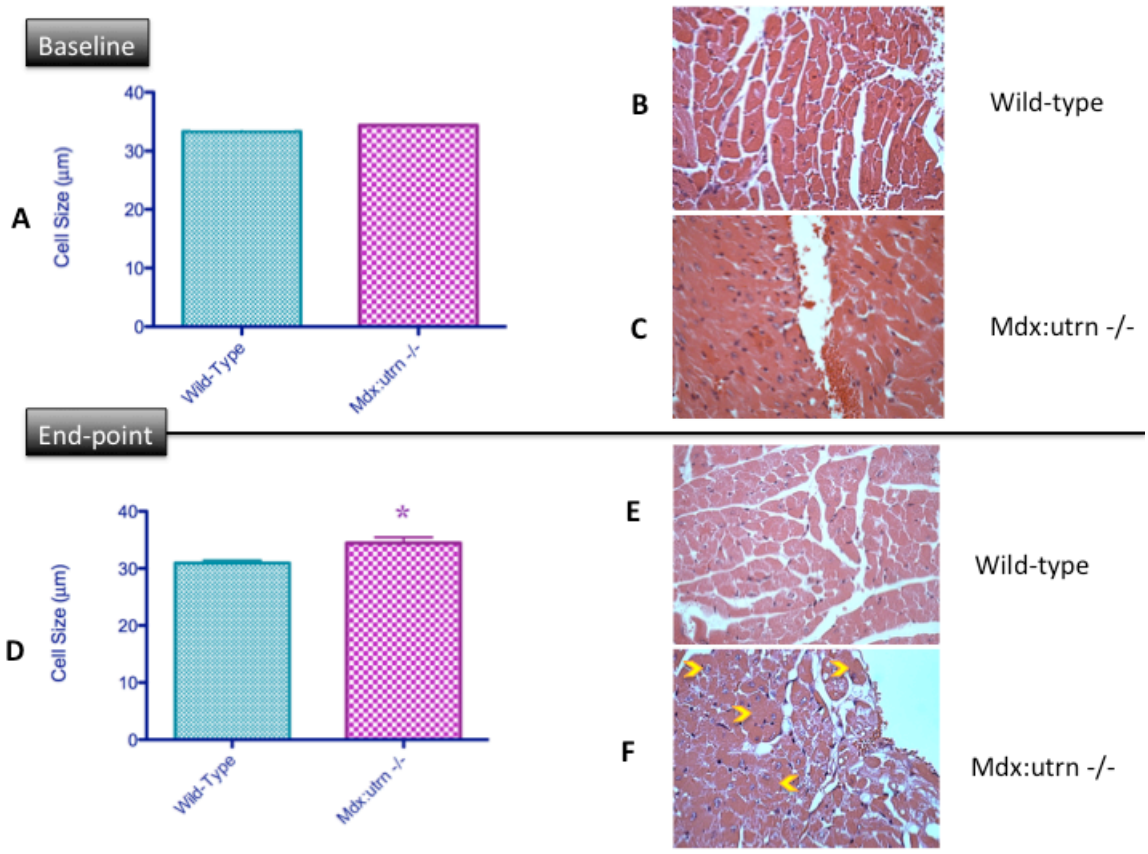

Figure 3.7: cardiomyocyte size (cell size) quantification to assess cardiomyocyte hypertrophy. Baseline (n=2 for mdx:utrn-/- and n=3 for wild-type). Endpoint (n=3 for mdx:utrn-/- and n=3 for the wild-type)
A) Quantification of cardiomyocytes size in mdx:utrn -/- and wild-type mice sacrificed at baseline. Low sample size in our mdx:utrn -/- group prevented inference of statistical relevance. B) H&E stained images of the left myocardium of wild-type mouse (taken at baseline) under 40X magnification. C) H&E stained images of the left myocardium of mdx:utrn-/- mouse (taken at baseline) under 40X magnification. D) Quantification of cardiomyocytes size in mdx:utrn -/- and wild-type mice sacrificed at end of study (endpoint). Unpaired T-test shows significantly higher cell size in the mdx:utrn-/- mice compared to wild-type mice ($P<0.05$) E) H&E stained images of the left myocardium of wild-type mouse (taken at endpoint) under 40X magnification. F) H&E stained images of the left myocardium of mdx:utrn-/- mouse (taken at endpoint) under 40X magnification. Yellow arrow tips depicts areas of cardiomyocytes hypertrophy.

Quantification of cardiac fibrosis were conducted at two time points of baseline and at the end of the study (Figure 3.6). Significantly higher cardiac fibrosis was observed in mdx:utrn-/- mice group at termination of study (9.4% cardiac fibrosis) when compared to wild-type mice (1.7% cardiac fibrosis)(P=0.0388). Quantification of cardiomyocytes size (cardiomyocytes hypertrophy assessment) were conducted at the two time points of baseline and end of study (Figure 3.7). Significantly higher cardiomyocyte size was observed in mdx:utrn -/- mice group (average of 34μm at end point) when compared to age matched wild-type mice (average of 31μm) at end point (P=0.0328). Low sample size in our mdx:utrn -/- group prevented inference of statistical relevance at baseline for fibrosis and cell size quantification.

CHAPTER 4:
DISCUSSION/CONCLUSION/LIMITATIONS/FUTURE DIRECTIONS

4.0 Discussion

Duchenne muscular dystrophy (DMD) is an X-linked recessive neuromuscular disease that results from a loss of functional dystrophin, leading to cardiomyocyte death, fibrosis, and dilated cardiomyopathy. In this thesis, I have utilized dynamic contrast enhanced computed tomography (DCE-CT), positron emission tomography (PET-FDG), echocardiography, and traditional histology to longitudinally assess disease progression and degree of cardiomyopathy in a murine model of DMD (mdx:utrn -/- mice) and compared these results to a control group (wild-type mice).

Use of DCE-CT, PET-FDG, and echocardiography each have distinct advantages and drawbacks to their use. One of the main advantages of functional CT over other modalities has been its simplicity and accessibility to patients. However, one of the drawbacks of CT is the high dose of radiation delivered to the body(71). Previously, PET has been used as the gold standard to validate new imaging techniques (ex. MRI) (85-89). Advantages of using PET include its high sensitivity, and it usefulness to illustrate organ functionality. However, the disadvantage of PET is exposure to ionizing radiation. Echocardiography benefits include low operating cost, lack of ionizing radiation, short scan times, and the ability for images to be captured in real time. One of the drawbacks of the diagnostic ultrasound is its operator dependence (operational variability that is introduced by the operator).

Given reports by Perloff et al. (1984) and Quinlivan et al. (1996), in which they assessed myocardial perfusion and metabolism in DMD patients (18,44), we sought to assess these parameters in dystrophic mice using DCE-CT, and PET-FDG. Despite observing a significant difference in the survival fraction of mdx:utrn-/-, relative to healthy mice, I did not observe significant changes in the myocardial blood flow, and blood volume as measured via DCE-CT (Figure 3.2 a,b). Standard uptake value of glucose (ie. metabolism) in the left myocardium was similarly unaffected over time (Figure 3.4). Furthermore, I did not observe significant difference in the CT-measured cardiac volume over time. Surprisingly, these results are not in parallel with previous cardiac studies that utilized PET to assess perfusion and metabolism in human DMD patients. Specifically, using PET-FDG and PET-NH_3, Perloff et al. (1984) measured metabolism and perfusion in the left ventricular myocardium of DMD patients. They found, that in 11 out of 12 patients there was an increase in glucose utilization in the areas of posteriobasal and posteriolateral walls of the left ventricle. Perloff et al. (1984) further demonstrated that in 13 out of the 15 DMD patients there was a reduction in $^{13}NH_3$ activity. Thus, they suggested that this increase in glucose uptake may be due to a segmental alteration in the permeability of the membrane in addition to a possible increase in glycolysis of glucose in response to decrease in utilization of fatty acids by the myocardium. Decrease in the ^{13}N activity in the myocardium is speculated to be possibly due to a metabolic abnormality, which causes reduction in the trapping or regional decrease in blood flow (18).

Radioactive PET tracers of FDG and NH_3 have been used in a similar study conducted by Quinlivan et al (1996). The authors demonstrate regional perfusion and metabolic defects in the left ventricular myocardium (in regions of lateral, apex, and anterior wall) in 15 out of 31 patients scanned. Out of the 15 patients, 11 exhibited regional defects in perfusion in the lateral wall of the left ventricle (out of these 11 patients, 9 showed a decrease in perfusion and increase in glucose metabolism, whereas 3 showed a decrease in both perfusion and metabolism). These findings led this group of researchers, to speculate that a decrease in both perfusion and glucose metabolism may be a sign of infarcted myocardium, whereas an increase in glucose metabolism in conjunction with decrease in blood flow may be due to ischemia of the myocardium (44).

The absence of dystrophin appears to have different effects on the myocardium than on skeletal muscle in murine models of DMD. Earlier studies conducted in our laboratory by Ahmad et al. (2011) utilized DCE-CT, and PET-FDG to study perfusion and metabolism respectively in the skeletal muscle of mdx mice, and severely effected mdx:utrn-/- mice. Initial observations showed an increase in perfusion (in both blood flow and blood volume) and glucose metabolism in the early stage of disease. A subsequent decrease in both parameters characterized by later stages of the disease is mostly evident in mdx:utrn -/- mice (in mdx mice, presence of utrophin compensates for the lack of dystrophin leading to a weak phenotype). The authors suggest that the initial increase could be due to a regeneration/degeneration cycle as apparent by the centrally located nuclei, a hallmark of regeneration. This peak of glucose metabolism alongside enhanced

perfusion was not observed in my myocardial study. Ahmad et al. (2011) further suggests, that the later decrease in perfusion and glucose metabolism may be due to necrosis and fibrosis (9).

Differences between my findings and earlier studies assessing perfusion and metabolism in DMD patients may reflect differences between humans and dystrophic mice. Furthermore, there may be a difference in utilization of various imaging metabolites when used to assess myocardial perfusion. In addition, at the time of earlier studies in DMD patients, cardiomyopathy might have been more severe than what is achieved in our mdx:utrn -/- mouse model. This is due to vast improvements in the palliative care, particularly in use of ventilatory support for DMD patients, which have increased their life expectancy.

As PET-FDG is the gold standard for assessing cardiac viability (90-93), it was not particularly surprising that we did not observe significant changes in the myocardial glucose uptake over time in the two groups of mice. Even though decreased cardiac function and fibrosis is present in midx:utrn -/- mice (shown through echocardiography and histology), the heart is still viable.

In a pilot study, I also sought to validate the use of echocardiography to assess the morphological/architectural and functional changes in dystrophic myocardia. Low sample size in our mdx:utrn -/- group prevented inference of statistical relevance. Overall, increasing trend in left ventricular internal diameter at systole was observed in mdx:utrn -/- mice from 5-7 weeks of age (baseline) to 15-17 weeks of age (end-point of study), compared to wild-type mice (where decreasing trend was observed). Furthermore, fractional shortening and ejection

fraction were observed to have an increasing trend in the wild-type mice. In contrast, a decreasing trend was observed in these two echocardiography parameters in mdx:utrn-/- mice from baseline to the end-point of my study.

Ejection fraction represents the volumetric fraction of blood that is pumped out of the heart in a cardiac cycle. A decrease in its value would indicate, that following each cardiac cycle, there is more volume of blood that is left in the ventricle following diastole, and hence can be translated to decreased function of the heart. In humans, ejection fraction ranges from 55%-77% (94); this is a range that was also observed in our wild-type mice (62% at baseline and 72% at end point) (Table 1). This was observed to be lower in the mdx:utrn -/- mice at 15-17 weeks of age (31%), possibly reflecting decreased function of the heart (94).

Fractional shortening is a slightly different way of measuring cardiac performance and represents the change in the functional diameter of the ventricle following cardiac cycle. A decrease in fractional shortening would mean that the rate of change of ventricular diameter is decreased, which is also translated to decreased cardiac function. In humans, fractional shortening ranges from 30% to 42% (95,96), with 26% to 30% representing decreased cardiac function (95,96); this is a range that was also observed in our wild-type mice (30% at baseline and 40% at endpoint) (95,96) (Table 1). However, it was observed that this value was lower in mdx:utrn-/- mice at 15-17 weeks of age(14%), possibly reflecting decreased function of the heart.

My findings support a very recent study involving mdx:utrn-/- mice conducted by Chun et al. (2012), where they utilized echocardiography and

histological analysis to study cardiac pathology and dysfunction during development of dilated cardiomyopathy in mdx:utrn -/- vs. wild-type mice. Echocardiography data did not show salient differences between the two mouse models by 5 weeks of age. However, they found dilation of the left ventricle, increase in the end systolic and diastolic volume, increase in left ventricular internal diameter and thinning of posterior ventricular wall by 15 weeks of age. Furthermore decreased ejection fraction and fractional shortening in the left ventricle was also observed (63).

Similarly, other echocardiography studies conducted by Spurney et al. (2008) and Quinlan et al. (2004) on mdx and healthy wild-type mice have found no significant changes in cardiac functional parameters in the first 2-3 months. However, a decrease in cardiac function was observed in mdx mice starting at 7-9 months of age. They both observed significant decrease in ejection fraction and fractional shortening by 7-9 month of age. Furthermore, Spurney et al. (2008), observed an increase in the left ventricular internal diameter at systole, and a decrease in left ventricular posterior wall thickness at systole. When compared to healthy wild-type mice, mdx mice showed decreased diastolic and mean blood pressure (97). In addition to a decrease in ejection fraction and fractional shortening, Quinlan et al. (2004) also observed a greater LV mass in the mdx mice by the age of 29 weeks. Furthermore, dilated cardiomyopathy was evident by 42 weeks of age in the mdx mice (32).

There are similarities in echocardiographic findings between the human DMD condition and mouse models. Specifically, in a study conducted by Nigro et al.

in 1990 and in his previous study in 1983, it was demonstrated that left ventricular function is normal in DMD patients under 6 years of age. However, there was a steady increase in the incidence of cardiomyopathy with age. By 18 years of age, there was evidence of contractile dysfunction with 72%, and 26% of patients having dilated cardiomyopathy and hypertrophic cardiomyopathy respectively. Furthermore they observed a decrease in fractional shortening, ejection fraction. (16,32,63,98). This is similar to the trend that was observed in my echocardiography pilot study.

In other echocardiography studies involving DMD patients, Danlilowicks et al. (1980), Golberg et al. (1982), and Melacini et al. (1996) have found similar cardiac functional abnormalities. Danilowicks et al. (1980), observed dilated left ventricle in 14 of the 36 patients scanned. Moreover, ventricular relaxation was low in 35 out of the 36 patients. They also observed a decrease in the ejection fraction in 30 patients(67). Golberg et al. (1982) observed that most DMD patients have contraction abnormality, which was initially seen in the posterior free wall of the left ventricle(66). Melacini et al. (1996) found that there are two patterns of cardiac involvement in advanced DMD: abnormalities in the wall motion in the left ventricle in addition to left ventricular dilation with reduced ejection fraction (64).

Overall, there are similarities and overlapping echocardiography findings in between our mouse model and the DMD condition observed in patients, which would make this model appropriate for assessing future treatments and monitoring the progression of disease.

An obvious and necessary component of my thesis is a correlation of non-invasive assessment of cardiomyopathy via DCE-CT, PET-FDG, and echocardiography, with histological analysis. In this study, I specifically conducted H&E staining to assess/quantify hypertrophy (cell size), and Masson's Trichrome staining to assess/quantify myocardial fibrosis. I found that fibrosis is significantly higher in mdx:utrn -/- mice compared to age matched wild-type mice at termination of study (Figure 3.6) (9.5% for mdx:utrn -/- , and 1.7% for wild-type mice). This demonstrates that cardiac fibrosis increases in the mdx:utrn -/- mice, whereas in wild type mice, fibrosis stays relatively constant . This is evidence of a deteriorating condition of myocardia mdx:utrn -/- mice. Quantification of cardiomyocyte size demonstrated significantly greater size in mdx:utrn -/- mice (average of 34μm at end point) relative to age matched wild-type mice (average of 31μm) in myocardia harvested at the termination of the study. This further suggests that cardiomyocyte hypertrophy might indeed dominate the later stages of myocardial disease in mice. This, in conjunction with an increasing trend in cardiac fibrosis, likely accelerates the deterioration of function in the heart.

Cardiac hypertrophy seems to dominate the focus of previous research rather than cardiomyocyte hypertrophy, and to our knowledge they have not been quantified before for DMD. However, Quinlan et al. (2004) mentioned that they have observed cardiomyocyte hypertrophy in mdx mice, but they have not presented the data for their finding(32). In a histopathology study of the heart in DMD patients, Frankel and Rosser (1976) have acknowledged presence of hypertrophy in the myocardium. However no quantification of this parameter was done (99).

Our fibrosis quantification findings are supported by a previously-mentioned study conducted by Chun et al. (2012), where fibrosis was detected in the outer regions of the ventricular wall and septum. By the age of 15 weeks, they observed approximately 17 times greater fibrosis than 5 weeks old mdx:utrn-/- mice(63). Similarly Spurney et al. (2008) and Quinlan et al. (2004) have quantified fibrosis in mdx mice. Spurney et al. (2008) have shown that there is approximately 6 times greater fibrosis in left ventricular myocardium of 9-10 month old mdx mice compared to the wild-type mice (100). Through quantifying fibrosis on 17 weeks old mdx mice, Quinlan et al. (2004) have shown almost 4 times greater fibrosis (with mdx mice having total 8% fibrosis) in the heart compared to the age matched wild-type mice. Also, they mentioned that there is a patchy pattern of fibrosis, which are evenly distributed and involve endocardium, myocardium and pericardium (32).

There are overlapping similarities in histological quantification findings between the human DMD condition and our mouse model. Overall, it appears that fibrosis is more extensive in DMD patients. Autopsy studies in DMD (99,101) did not quantify the degree of the fibrosis, however their narrative description suggests presence of severe fibrosis in areas of posteriobasal, anterolatleral, and inferoposterior of left ventricular walls.

4.1 Conclusion

Most significant findings of this thesis are as follows:

1) Dynamic contrast enhanced computed tomography (DCE-CT), and positron emission tomography (PET-FDG) demonstrates that myocardial perfusion

(blood flow and blood volume) and metabolism is not affected in the mdx:utrn-/- mice relative to healthy wild-type mice.

2) Pilot echocardiography data shows possible decrease in cardiac function of mdx:utrn -/- compared to age matched wild-type by 15-17 weeks of age. Decreasing trend was observed in ejection fraction and fractional shortening, alongside increasing trend in systolic left ventricular internal diameter in mdx:utrn -/- mice. These findings supports previous studies and possibly validates utility of echo to reproducibility assess cardiac disease progression in mouse models.
3) Histological quantification analysis shows significant increase in cardiac fibrosis in mdx:utrn -/- mice compared to wild-type at termination of study. Also cardiomyocytes size (cell size) quantification showed that there is significant increase in cell size in mdx:utrn-/- mice at the end point of study. Histological quantification analysis allows important correlation to non-invasive assessment of cardiomyopathy, using imaging methods that are as of yet unvalidated in small animals preclinical models.

4.2 Limitations

One of the limitations of our study may have been my utilization of clinical CT. Clinical CT provided me with image slices of 1.25 mm thickness, which might not have been sufficient for the detailed analysis of the mouse myocardium. Furthermore, this slice thickness might have provided me with inaccurate calculation of cardiac volume, as few slices were available to be analyzed. In addition, clinical CT provided me with transaxial resolution that limited accurate

delineation of the boundaries of the chambers; hence calculation of the whole cardiac volume was done (calculation of left ventricular volume would have been more optimal as dilated cardiomyopathy largely effects the left ventricle).

Another limitation of the study involved echocardiography. Measurement of cardiac ejection fraction was not precise, as it involved approximate volumetric calculation of the left ventricle using Teichholz equation. In addition, variability introduced by the operator could affect the results. Accuracy of the parameter measurements in the longitudinal study was dependent on the expertise of the operator to obtain consistent M-mode beam placement for the echocardiography parameter measurements at different time points.

In addition, survival rate of the mice could be affected by the radiation given during the scans to the mice via CT and PET. However, since wild-type mice did not exhibit overt cardiac muscle damage, this can be possibly ruled out.

4.3 Future Directions

Some future directions of our lab's research may be to use the findings of this study as a baseline to assess the efficacy of various treatments and to improve our fundamental understanding of the progression of the disease. In the near future, our group is also considering the use of gated micro computed tomography to assess its capability to characterize the progression of cardiomyopathy in mdx:utrn -/- vs. wild-type mice. Gated micro computed tomography could be utilized to calculate ejection fraction with higher degree of accuracy by actual ventricular volume measurement (region growing using seed and thresholding) at the two phases of diastole and systole. Furthermore, our group is considering performing a

reproducibility study (involving scanning of healthy mice in time), to assess consistency of the echocardiography measurements.

In addition a statistical power analysis will be conducted in near future to determine the appropriate sensitivity of the three modalities used in the study. The results of this would aid us in choosing the optimal modality that can be utilized for assessing and monitoring of the success/failure of future therapeutics. Furthermore, our group is also considering other means of assessing myocardial disease progression in our murine model of DMD via positron emission tomography using new myocardial perfusion tracers. Our long-term goal is to use these findings to determine the efficacy of stem cell therapy in regeneration of cardiomyocytes. We are hoping that current and future findings can be translated to better treatments and more accurate monitoring of disease progression in DMD patients.

REFERENCES:

1. Lu QL, Rabinowitz A, Chen YC, Yokota T, Yin HF, Alter J, et al. Systemic delivery of antisense oligoribonucleotide restores dystrophin expression in body-wide skeletal muscles. Proceedings of the National Academy of Sciences. 2005;102(1):198-203.

2. De Angelis FG, Sthandier O, Berarducci B, Toso S, Galluzzi G, Ricci E, et al. Chimeric snRNA molecules carrying antisense sequences against the splice junctions of exon 51 of the dystrophin pre-mRNA induce exon skipping and restoration of a dystrophin synthesis in Δ48-50 DMD cells. Proceedings of the National Academy of Sciences. 2002;99(14):9456-9461.

3. Haslett JN, Sanoudou D, Kho AT, Bennett RR, Greenberg SA, Kohane IS, et al. Gene expression comparison of biopsies from Duchenne muscular dystrophy (DMD) and normal skeletal muscle. Proceedings of the National Academy of Sciences. 2002;99(23):15000-15005.

4. Kim TW, Wu K, Xu J, Black IB. Systemic delivery of antisense oligoribonucleotide restores dystrophin expression in body-wide skeletal muscles. Proceedings of the National Academy of Sciences. 1992;89(23):11642.

5. Acsadi G, Dickson G, Love DR, Jani A, Walsh FS, Gurusinghe A, et al. Human dystrophin expression in mdx mice after intramuscular injection of DNA constructs. 1991;352:815–818.

6. Nudel U, Robzyk K, Yaffe D. Expression of the putative Duchenne muscular dystrophy gene in differentiated myogenic cell cultures and in the brain. 1988;331:635–638.

7. Ray PN, Belfall B, Duff C, Logan C, Kean V, Thompson MW, et al. Cloning of the breakpoint of an X; 21 translocation associated with Duchenne muscular dystrophy. 1985;318:672–675.

8. Iannaccone S. Current status of Duchenne muscular dystrophy. Pediatric clinics of North America. 1992;39(4):879-894.

9. Ahmad N, Welch I, Grange R, Hadway J, Dhanvantari S, Hill D, et al. Use of imaging biomarkers to assess perfusion and glucose metabolism in the skeletal muscle of dystrophic mice. BMC Musculoskeletal Disorders. 2011 Jun. 4;12(1):127.

10. Jay V, Vajsar J. The dystrophy of Duchenne. The Lancet.

2001;357(9255):550.

11. Bonilla E, Samitt CE, Miranda AF, Hays AP, Salviati G, DiMauro S, et al. Duchenne muscular dystrophy: deficiency of dystrophin at the muscle cell surface. Cell. 1988;54(4):447–452.

12. Campbell KP. Three Muscular Dystrophies: Review Loss of Cytoskeleton-Extracellular Matrix Linkage. Cell. 1995;80:675–679.

13. Ohlendieck K, Matsumura K, Ionasescu V, Towbin J, Bosch E, Weinstein S, et al. Duchenne muscular dystrophy. Neurology. 1993;43(4):795–795.

14. Wallace GQ, McNally EM. Mechanisms of muscle degeneration, regeneration, and repair in the muscular dystrophies. Annu. Rev. Physiol. 2009;71:37–57.

15. Towbin JA. The role of cytoskeletal proteins in cardiomyopathies. Current opinion in cell biology. 1998;10(1):131–139.

16. Nigro G, Comi L, Politano L, Bain R. The incidence and evolution of cardiomyopathy in Duchenne muscular dystrophy. International journal of cardiology. 1990;26(3):271–277.

17. Deconinck AE, Rafael JA, Skinner JA, Brown SC, Potter AC, Metzinger L, et al. Utrophin-dystrophin-deficient mice as a model for Duchenne muscular dystrophy. Cell. 1997;90(4):717–727.

18. Perloff J, Henze E, Schelbert H. Alterations in regional myocardial metabolism, perfusion, and wall motion in Duchenne muscular dystrophy studied by radionuclide imaging. Circulation. 1984;69(1):33–42.

19. Grady RM, Teng H, Nichol MC, Cunningham JC, Wilkinson RS, Sanes JR. Skeletal and cardiac myopathies in mice lacking utrophin and dystrophin: a model for Duchenne muscular dystrophy. Cell. 1997;90(4):729–738.

20. Heymsfield S, McNish T, Perkins J, Felner J. Sequence of cardiac changes in Duchenne muscular dystrophy. American heart journal. 1978;95(3):283–294.

21. Puchalski MD, Williams RV, Askovich B, Sower CT, Hor KH, Su JT, et al. Late gadolinium enhancement: precursor to cardiomyopathy in Duchenne muscular dystrophy? The International Journal of Cardiovascular Imaging (formerly Cardiac Imaging). 2009;25(1):57–63.

22. Mulder BJM, van der Wall EE. Duchenne muscular dystrophy; a cardiomyopathy that can be prevented? The International Journal of Cardiovascular Imaging (formerly Cardiac Imaging). 2009;25(1):65–67.

23. McNally EM. Duchenne muscular dystrophy: how bad is the heart? Heart. 2008;94(8):976–977.

24. Pinnell J, Turner S, Howell S. Cardiac muscle physiology.

25. Fearnley CJ, Roderick HL, Bootman MD. Calcium Signaling in Cardiac Myocytes. Cold Spring Harbor Perspectives in Biology. 2011;3(11):a004242.

26. Bers DM. Calcium cycling and signaling in cardiac myocytes. Annu. Rev. Physiol. 2008;70:23–49.

27. Berridge M, Lipp P, Bootman M. Calcium signalling. Current biology. 1999;9(5):157–159.

28. Manyari DE, Klein GJ, Gulamhusein S, Boughner D, Guiraudon GM, Wyse G, et al. Arrhythmogenic right ventricular dysplasia: a generalized cardiomyopathy? Circulation. 1983;68(2):251–257.

29. Kushwaha SS, Fallon JT, Fuster V. Restrictive cardiomyopathy. New England Journal of Medicine. 1997;336(4):267–276.

30. Maron BJ. Hypertrophic cardiomyopathy. JAMA: the journal of the American Medical Association. 2002;287(10):1308–1320.

31. Maron BJ. Hypertrophic cardiomyopathy. The Lancet. 1997;350(9071):127–133.

32. Quinlan JG, Hahn HS, Wong BL, Lorenz JN, Wenisch AS, Levin LS. Evolution of the mdx mouse cardiomyopathy: physiological and morphological findings. Neuromuscular Disorders. 2004 Sep.;14(8-9):491–496.

33. Kärkkäinen S, Peuhkurinen K. Genetics of dilated cardiomyopathy. Annals of medicine. 2007;39(2):91-107.

34. Darras BT, Korf B, Urion DK. Dystrophinopathies. 1993;

35. Sultan A, Fayaz M. Prevalence of cardiomyopathy in Duchenne and Becker's muscular dystrophy. J Ayub Med Coll Abbottabad. 2008;20(2):7–13.

36. Oldfors A, Eriksson B, Kyllerman M, Martinsson T, Wahlström J. Dilated cardiomyopathy and the dystrophin gene: an illustrated review. Heart. 1994;72(4):344–348.

37. Emery AEH, Muntoni F. Duchenne muscular dystrophy. 1993;392.

38. Verma S, Anziska Y, Cracco J. Review of Duchenne muscular dystrophy (DMD) for the pediatricians in the community. Clinical pediatrics. 2010;49(11):1011–1017.

39. Rideau Y, Jankowski L, Grellet J. Respiratory function in the muscular dystrophies. Muscle Nerve. 1981;4(2):155–164.

40. de Visser M, de Voogt WG, la Rivière GV. The heart in Becker muscular dystrophy, facioscapulohumeral dystrophy, and Bethlem myopathy. Muscle Nerve. 1992;15(5):591–596.

41. Danilowicz D, Rutkowski M, Myung D, Schievely D. Echocardiography in duchenne muscular dystrophy. Muscle Nerve. 1980 Jul.;3(4):298–303.

42. Engel A. Acquired autoimmune myasthenia gravis. Myology. New York: McGraw-Hill. 1994;:1769–1797.

43. Frankel KA, Rosser RJ. The pathology of the heart in progressive muscular dystrophy: epimyocardial fibrosis. Human pathology. 1976;7(4):375–386.

44. Quinlivan R, Lewis P, Marsden P, Dundas R, Robb S, Baker E, et al. Cardiac function, metabolism and perfusion in Duchenne and Becker muscular dystrophy. Neuromuscular Disorders. 1996;6(4):237–246.

45. Wehling-Henricks M. Cardiomyopathy in dystrophin-deficient hearts is prevented by expression of a neuronal nitric oxide synthase transgene in the myocardium. Human Molecular Genetics. 2005 May 25;14(14):1921–1933.

46. Ohlendieck K, Matsumura K, Ionasescu V, Towbin J, Bosch E, Weinstein S, et al. Duchenne muscular dystrophy. Neurology. 1993;43(4):795–795.

47. Jacobs PA, Hunt PA, Mayer M, Bart RD. Duchenne muscular dystrophy (DMD) in a female with an X/autosomal translocation: Further evidence that the DMD locus is at Xp21. American journal of human genetics. 1981;33(4):513-518.

48. Burghes AHM, Logan C, Hu X, Belfall B, Worton RG, Ray PN. A cDNA clone from the Duchenne/Becker muscular dystrophy gene. 1987;328:434–437.

49. Worton RG, Thompson MW. Genetics of Duchenne Muscular Dystrophy. Annu. Rev. Genet. 1988 Dec.;22(1):601–629.

50. Tennyson CN, Klamut HJ, Worton RG. The human dystrophin gene requires 16 hours to be transcribed and is cotranscriptionally spliced. Nat Genet. 1995 Feb.;9(2):184–190.

51. Blake DJ, Weir A, Newey SE, Davies KE. Function and genetics of dystrophin and dystrophin-related proteins in muscle. Physiological reviews. 2002;82(2):291–329.

52. Roberts RG. Dystrophins and dystrobrevins. Genome Biol. 2001;2(4):1–7.

53. Li H, Zhao L, Wu Y, Liu Q, Ji X. Expression of dystrophin–glycoprotein complex (DGC) in muscles from DMD patients: Overview of 80 cases (9 days–12 years of age). Abstracts/Neuromuscular Disorders. 2011;21:639–751.

54. Williams IA, Allen DG. Intracellular calcium handling in ventricular myocytes from mdx mice. Am J Physiol Heart Circ Physiol. 2007:846–854.

55. Kaspar RW, Allen HD, Montanaro F. Current understanding and management of dilated cardiomyopathy in Duchenne and Becker muscular dystrophy. Journal of the American Academy of Nurse Practitioners. 2009 May;21(5):241–249.

56. Mori K, Hayabuchi Y, Inoue M, Suzuki M, Sakata M, Nakagawa R, et al. Myocardial strain imaging for early detection of cardiac involvement in patients with Duchenne's progressive muscular dystrophy. Echocardiography. 2007;24(6):598–608.

57. Collins C, Morgan J. Duchenne's muscular dystrophy: animal models used to investigate pathogenesis and develop therapeutic strategies. International journal of experimental pathology. 2003;84(4):165–172.

58. Gaschen L, Lang J, Lin S, Adé Damilano M, Busato A, Lombard CW, et al. Cardiomyopathy in Dystrophin-Deficient Hypertrophic Feline Muscular Dystrophy. Journal of Veterinary Internal Medicine. 1999;13(4):346–356.

59. Bulfield G, Siller W, Wight P, Moore KJ. X chromosome-linked muscular dystrophy (mdx) in the mouse. Proceedings of the National Academy of Sciences. 1984;81(4):1189-1192.

60. Matsumura K, Campbell KP. Dystrophin–glycoprotein complex: its role in the molecular pathogenesis of muscular dystrophies. Muscle Nerve. 1994;17(1):2–15.

61. Chamberlain JS. Duchenne muscular dystrophy models show their age. Cell. 2010;143(7):1040–1042.

62. Megeney LA, Kablar B, Perry RLS, Ying C, May L, Rudnicki MA. Severe cardiomyopathy in mice lacking dystrophin and MyoD. Proceedings of the National Academy of Sciences. 1999;96(1):220-225.

63. Chun JL, O'Brien R, Berry SE. Cardiac dysfunction and pathology in the dystrophin and utrophin-deficient mouse during development of dilated cardiomyopathy. Neuromuscular Disorders. 2012;22(4):368–379.

64. Melacini P, Vianello A, Villanova C, Fanin M, Miorin M, Angelini C, et al. Cardiac and respiratory involvement in advanced stage Duchenne muscular

dystrophy. Neuromuscular Disorders. 1996 Oct.;6(5):367–376.

65. de Kermadec JM, Bécane HM, Chénard A, Tertrain F, Weiss Y. Prevalence of left ventricular systolic dysfunction in Duchenne muscular dystrophy: an echocardiographic study. American heart journal. 1994;127(3):618–623.

66. Goldberg SJ, Stern LZ, Feldman L, Allen HD, Sahn DJ, Valdes-Cruz LM. Serial two-dimensional echocardiography in Duchenne muscular dystrophy. Neurology. 1982;32(10):1101–1101.

67. Danilowicz D, Rutkowski M, Myung D, Schievely D. Echocardiography in duchenne muscular dystrophy. Muscle Nerve. 1980 Jul.;3(4):298–303.

68. Sasaki K, Sakata K, Kachi E, Hirata S, Ishihara T, Ishikawa K. Sequential changes in cardiac structure and function in patients with Duchenne type muscular dystrophy: a two-dimensional echocardiographic study. American heart journal. 1998;135(6):937–944.

69. CHETBOUL V, Escriou C, Tessier D, Richard V, Pouchelon JL, Thibault H, et al. Tissue Doppler imaging detects early asymptomatic myocardial abnormalities in a dog model of Duchenne's cardiomyopathy. European Heart Journal. 2004;25(21):1934–1939.

70. Spencer MJ, Tidball JG. Do immune cells promote the pathology of dystrophin-deficient myopathies? Neuromuscular Disorders. 2001;11(6-7):556–564.

71. Lee TY. Functional CT: physiological models. Trends in biotechnology. 2002;20(8):S3–S10.

72. Lawrence KSS, Lee TY. An adiabatic approximation to the tissue homogeneity model for water exchange in the brain: I. Theoretical derivation. Journal of Cerebral Blood Flow & Metabolism. 1998;18(12):1365–1377.

73. Sahani DV, Kalva SP, Hamberg LM, Hahn PF, Willett CG, Saini S, et al. Assessing Tumor Perfusion and Treatment Response in Rectal Cancer with Multisection CT: Initial Observations1. Radiology. 2005;234(3):785–792.

74. Johnson JA, Wilson TA. A model for capillary exchange. American Journal of Physiology--Legacy Content. 1966;210(6):1299–1303.

75. Schelbert HR, Phelps ME, Hoffman E, Huang SC, Kuhl DE. Regional myocardial blood flow, metabolism and function assessed noninvasively with positron emission tomography. The American Journal of Cardiology. 1980;46(7):1269–1277.

76. Ter-Pogossian MM, Phelps ME, Hoffman EJ, Mullani NA. A positron-emission transaxial tomograph for nuclear imaging (PETT). Radiology. 1975;114(1):89–98.

77. Townsend DW. Positron emission tomography/computed tomography. Seminars in nuclear medicine. 2008;38(3):152–166.

78. Berger A. How Does It Work? Positron Emission Tomography. BMJ: British Medical Journal. 2003 Jan. 28;326(7404):1449.

79. Bengel FM, Higuchi T, Javadi MS, Lautamäki R. Cardiac positron emission tomography. Journal of the American College of Cardiology. 2009;54(1):1–15.

80. Garbi M. The general principles of echocardiography [Internet]. In: Fox K, Sicari R, Zamorano JL, Badano L, editors. The EAE Textbook of Echocardiography. 2011. p. 1–14.Available from: http://oxfordmedicine.com/view/10.1093/med/9780199599639.001.0001/med-9780199599639

81. LEIGHTON T. What is ultrasound? Progress in Biophysics and Molecular Biology. 2007 Jan.;93(1-3):3–83.

82. WRITING COMMITTEE MEMBERS, Hendel RC, Budoff MJ, Cardella JF, Chambers CE, Dent JM, et al. ACC/AHA/ACR/ASE/ASNC/HRS/NASCI/RSNA/SAIP/SCAI/SCCT/SCMR/SIR 2008 Key Data Elements and Definitions for Cardiac Imaging: A Report of the American College of Cardiology/American Heart Association Task Force on Clinical Data Standards (Writing Committee to Develop Clinical Data Standards for Cardiac Imaging). Circulation. 2009 Jan. 5;119(1):154–186.

83. Xiang FL, Lu X, Hammoud L, Zhu P, Chidiac P, Robbins J, et al. Cardiomyocyte-specific overexpression of human stem cell factor improves cardiac function and survival after myocardial infarction in mice. Circulation. 2009;120(12):1065–1074.

84. Gao XM, Agrotis A, Autelitano DJ, Percy E, Woodcock EA, Jennings GL, et al. Sex hormones and cardiomyopathic phenotype induced by cardiac β2-adrenergic receptor overexpression. Endocrinology. 2003;144(9):4097–4105.

85. Knuesel PR, Nanz D, Wyss C, Buechi M, Kaufmann PA, Schulthess von GK, et al. Characterization of dysfunctional myocardium by positron emission tomography and magnetic resonance. Circulation. 2003;108(9):1095–1100.

86. Klein C, Nekolla SG, Bengel FM, Momose M, Sammer A, Haas F, et al.

Assessment of myocardial viability with contrast-enhanced magnetic resonance imaging. Circulation. 2002;105(2):162–167.

87. Schwitter J, DeMarco T, Kneifel S, Schulthess von G, Jörg MC, Arheden H, et al. Magnetic resonance–based assessment of global coronary flow and flow reserve and its relation to left ventricular functional parameters: a comparison with positron emission tomography. Circulation. 2000;101(23):2696–2702.

88. Baer FM, Voth E, Schneider CA, Theissen P, Schicha H, Sechtem U. Comparison of Low-Dose Dobutamine–Gradient-Echo Magnetic Resonance Imaging and Positron Emission Tomography With [18F] Fluorodeoxyglucose in Patients With Chronic Coronary Artery Disease: A Functional and Morphological Approach to the Detection of Residual Myocardial Viability. Circulation. 1995;91(4):1006–1015.

89. Dilsizian V, Arrighi JA, Diodati JG, Quyyumi AA, Alavi K, Bacharach SL, et al. Myocardial viability in patients with chronic coronary artery disease. Comparison of 99mTc-sestamibi with thallium reinjection and [18F] fluorodeoxyglucose [published erratum appears in Circulation 1995 Jun 15; 91 (12): 3026]. Circulation. 1994;89(2):578–587.

90. Döbert N, Britten M, Assmus B, Berner U, Menzel C, Lehmann R, et al. Transplantation of progenitor cells after reperfused acute myocardial infarction: evaluation of perfusion and myocardial viability with FDG-PET and thallium SPECT. European journal of nuclear medicine and molecular imaging. 2004;31(8):1146–1151.

91. Bax JJ, Visser FC, Lingen A, Cornel JH, Fioretti PM, van der Wall EE. Metabolic imaging using F18-fluorodeoxyglucose to assess myocardial viability. The International Journal of Cardiac Imaging. 1997;13(2):145–155.

92. Keng F. Clinical applications of positron emission tomography in cardiology: a review. ANNALS-ACADEMY OF MEDICINE SINGAPORE. 2004;33(2):175–182.

93. Perrone-Filardi P, Bacharach S, Dilsizian V, Maurea S, Frank J, Bonow R. Regional left ventricular wall thickening. Relation to regional uptake of 18fluorodeoxyglucose and 201Tl in patients with chronic coronary artery disease and left ventricular dysfunction. Circulation. 1992;86(4):1125–1137.

94. Sutton P. Measurements in cardiology. 1999;

95. Lang RM, Bierig M, Devereux RB, Flachskampf FA, Foster E, Pellikka PA, et al. Recommendations for chamber quantification. European Journal of Echocardiography. 2006;7(2):79–108.

96. Borow KM, Green LH, Grossman W, Braunwald E. Left ventricular end-systolic stress-shortening and stress-length relations in humans: normal values and sensitivity to inotropic state. The American Journal of Cardiology. 1982;50(6):1301–1308.

97. Spurney CF, Knoblach S, Pistilli EE, Nagaraju K, Martin GR, Hoffman EP. Dystrophin-deficient cardiomyopathy in mouse: expression of Nox4 and Lox are associated with fibrosis and altered functional parameters in the heart. Neuromuscular Disorders. 2008;18(5):371–381.

98. Nigro G, Comi LI, Limongelli FM, Giugliano MAM, Politano L, Petretta V, et al. Prospective study of X-linked progressive muscular dystrophy in campania. Muscle Nerve. 1983 May;6(4):253–262.

99. Frankel KA, Rosser RJ. The pathology of the heart in progressive muscular dystrophy: epimyocardial fibrosis. Human pathology. 1976;7(4):375–386.

100. Spurney CF. Cardiomyopathy of duchenne muscular dystrophy: Current understanding and future directions. Muscle Nerve. 2011;44(1):8–19.

101. Nishimura T, Yanagisawa A, Sakata H, Sakata K, Shimoyama K, Ishihara T, et al. Thallium-201 single photon emission computed tomography (SPECT) in patients with duchenne's progressive muscular dystrophy: a histopathologic correlation study. Japanese circulation journal. 2001;65(2):99-105.

APPENDIX

AUSPC

From:
Sent: Thursday, September 01, 2011 10:34 AM
To:
Cc:
Subject: eSirius Notification - Annual Protocol Renewal APPROVED by the AUS 2008-067::3

AUP Number: 2008-067
PI Name: Hoffman, Lisa M
AUP Title: Non-Invasive Imaging of Therapeutics in Mouse Models of DMD

The YEARLY RENEWAL to Animal Use Protocol (AUP) 2008-067 has been approved.

1. This AUP number must be indicated when ordering animals for this project.
2. Animals for other projects may not be ordered under this AUP number.
3. Purchases of animals other than through this system must be cleared through the ACVS office. Health certificates will be required.

REQUIREMENTS/COMMENTS
Please ensure that individual(s) performing procedures on live animals, as described in this protocol, are familiar with the contents of this document.

The holder of this Animal Use Protocol is responsible to ensure that all associated safety components (biosafety, radiation safety, general laboratory safety) comply with institutional safety standards and have received all necessary approvals. Please consult directly with your institutional safety officers.

Submitted by: Thompson, Sharla H
on behalf of the Animal Use Subcommittee

The University *of* Western Ontario
Animal Use Subcommittee / University Council on Animal Care
Health Sciences Centre, ● London, Ontario ● CANADA – N6A 5C1
PH: 519-661-2111 ext. 86768 ● FL 519-661-2028
Email: auspam@uwo.ca ● http://www.uwo.ca/animal/website/

CURRICULUM VITAE

NAME: **Seyed Hamed Moazami**

EDUCATIONAL BACKGROUND

- **University of Western Ontario,** *London, Ontario: (09/2010 to present)*
  MSc. Medical Biophysics
  Thesis: **"***Stem Cell Therapy for the Treatment of Duchenne Muscular Dystrophy-related cardiomyopathy."*
- **Ryerson University,** *Toronto, Ontario: (09/2007 to 07/2010)*
  Honours B.Sc. Medical Physics
  Honors Thesis: *"Protoporphyrin IX Synthesis From Aminolevulinic Acid In Brain Tumor Cells Under Different Growth Conditions And Its influence in Photodynamic Therapy."*
- **University of Toronto,** *Toronto, Ontario: (09/2003 to 06/2007)*
  B.Sc. Integrative Biology

AWARDS AND ACHIEVEMENTS

- **Translational Breast Cancer Studentship from the London Regional Cancer Program** (2010)- Competitive Fellowship awarded for the value of $22,138
- **Schulich Graduate Scholarship(SGS)**(2010-2012)- awarded for high academic standing for the value of $6788.
- **Ryerson University Dean's List** (*2007-2009*)-Maintained cumulative average above 80%.
- **McMaster University Civil Arm Olympics:** Obtained 3rd place award in bridge model competitions (*10/2002*).

LEADERSHIP AND TEACHING EXPERIENCE

- **Medical Biophysics Teaching Assistant**
  University of Western Ontario,London,Ontario (for Dr. Daniel Goldman & Dr. Christopher G. Ellis) *(01/2011 to 04/2012)*
  - (Part-time) In charge of the Tutorial section of the biophysical analysis of oxygen transport in biological system course (Medical Biophysics 3507). This included instructing students in relevant tutorial course materials, as well as marking of assignments.
- **Medical Physics Teaching Assistant**
  Ryerson University,Toronto,Ontario (for Dr. T. Antimirova) *(01/2009 to 04/2010)*
  - (Part-time) In charge of the laboratory section of the Electricity and Magnetism course (PCS 228). This included instructing students in relevant laboratory course materials, assisting students in conducting the labs, and marking of the course lab materials.

- **Tutoring**
  Premium Tutoring, NorthYork, Ontario (*04/2005 to 04/2007*)
  - (Part-time) Tutoring individuals and classes in the subject of Mathematics, Physics, Chemistry and Biology.
  - Advising an preparation of students for the SAT Exams.

RESEARCH EXPERIENCE

- **Medical Physics Summer Research Assistant**
  Ryerson University, Toronto, Ontario (for Dr. M. Kolios) *(01/2008 07/2008)*
  - (Full-time) Non-invasive estimation of temperature at single cell level using acoustic microscopy. First method applied was use of zero crossing in Matlab to measure the change in the instantaneous frequency as function of time. The second method used the phase shift of the radio-frequency data using Matlab from the transducer to further calculate temperature.
  - Webmaster for the microscopy group.
- **Cognitive Neuroscience laboratory and Research Assistant**
  University of Toronto, Toronto, Ontario (*05/2006 to 08/2006*)
  - (Part-time) Conducting experiments focusing on attention based spatial tasks, by the use of Eye-link (Head mounted video based eye tracker).
- **Mount Sinai General Hospital**
  Mount Sinai Hospital, Toronto, Ontario (*04/2005 to 08/2005*)
  - Assisted nursing units, supported staff with divisional activities, clerical support, and related duties.

PRESENTATIONS

- London Health Research Day Poster Presentation, London, Ontario (March 2012)
  Title of presentation: *"Characterization of Cardiomyopathy in a Mouse Model of Duchenne Muscular Dystrophy (DMD) using Imaging Biomarkers."*
- Honors Thesis Department Poster Presentation, Toronto, Ontario *(April, 2010)*
  Title of presentation: *"Protoporphyrin IX Synthesis From Aminolevulinic Acid In Brain Tumor Cells Under Different Growth Conditions And Its influence in Photodynamic Therapy."*
- University of Prince Edward Island in collaboration with Ryerson University Computer Science, Engineering, Mathematics and Physics Undergraduate Research Symposium, Toronto, Ontario *(August 13, 2008).*
  Title of presentation: *"Non-invasive estimation of temperature at the single cell level using acoustic microscopy."*
  Co-Authors: Dr. Michael Kolios

TECHNICAL SKILLS

- Experienced in working with Acoustic, Optical, and Fluorescent Microscope, as well as Spectrofluorometer, and Bioluminescence.
- Experience in operating GE and Siemens Micro-PET scanner, and GE Clinical CT.
- Extensive experience working with Kibero signal analysis software.
- Experience in working with Matlab, Prism and SPSS statistical software.
- Cell Culturing (adhesive cell line), PCR, IHC, FACS.
- Use of Eye-link software to measure and manipulate spatial related tasks.